



**HAL**  
open science

## A Fukushima tracer perspective on four years of North Pacific mode water evolution

Alison M Macdonald, Sachiko Yoshida, Steven M Pike, Ken O Buesseler, Irina I Rypina, Steven R Jayne, Vincent Rossi, Jennifer Kenyon, Jessica A Drysdale

► **To cite this version:**

Alison M Macdonald, Sachiko Yoshida, Steven M Pike, Ken O Buesseler, Irina I Rypina, et al.. A Fukushima tracer perspective on four years of North Pacific mode water evolution. Deep Sea Research Part I: Oceanographic Research Papers, 2020, 166, pp.103379. 10.1016/j.dsr.2020.103379 . hal-02992261

**HAL Id: hal-02992261**

**<https://hal.science/hal-02992261>**

Submitted on 1 Dec 2021

**HAL** is a multi-disciplinary open access archive for the deposit and dissemination of scientific research documents, whether they are published or not. The documents may come from teaching and research institutions in France or abroad, or from public or private research centers.

L'archive ouverte pluridisciplinaire **HAL**, est destinée au dépôt et à la diffusion de documents scientifiques de niveau recherche, publiés ou non, émanant des établissements d'enseignement et de recherche français ou étrangers, des laboratoires publics ou privés.

# **A Fukushima tracer perspective on four years of North Pacific mode water evolution**

Alison M. Macdonald<sup>a\*</sup>, Sachiko Yoshida<sup>a</sup>, Steven M. Pike<sup>b</sup>, Ken O. Buesseler<sup>b</sup>, Irina I. Rypina<sup>a</sup>, Steven R. Jayne<sup>a</sup>, Vincent Rossi<sup>c,d</sup>, Jennifer Kenyon<sup>b</sup>, Jessica A. Drysdale<sup>b</sup>

<sup>a</sup> Woods Hole Oceanographic Institution, Physical Oceanography Department, Woods Hole, MA, USA

<sup>b</sup> Woods Hole Oceanographic Institution, Marine Chemistry and Geochemistry Department, Woods Hole, MA, USA

<sup>c</sup> Mediterranean Institute of Oceanography (UM 110, UMR 7294), CNRS, Aix Marseille Univ., Univ. Toulon, IRD, Marseille, 13288, France

<sup>d</sup> Climate Change Research Centre, University of New South Wales, Sydney, New South Wales, 2052, Australia

\* Corresponding author. WHOI MS21, 266 Woods Hole Rd., Woods Hole, MA 02543. E-mail address: [amacdonald@whoi.edu](mailto:amacdonald@whoi.edu) (A.M. Macdonald).

## 1 **Abstract**

2 We present the results of a multi-platform investigation that utilizes tracer information provided  
3 by the 2011 release of radioisotopes from the Fukushima Dai-ichi Nuclear Power Plant to better  
4 understand the pathways, mixing and transport of mode waters formed in the North Pacific Ocean.  
5 The focus is on transition region mode waters and radiocesium ( $^{137}\text{Cs}$  and  $^{134}\text{Cs}$ ) observations  
6 obtained from the May-June 2015 GO-SHIP occupation of the  $152^\circ\text{W}$  line in the Northeast Pacific.  
7 Samples include profiles from the surface to 1000 m and surface/subsurface pairs that provide an  
8 average  $1^\circ$  of latitude spacing along  $152^\circ\text{W}$ . We find a clear Fukushima ( $^{134}\text{Cs}$ ) signal from the  
9 surface to 400 m. The core signal ( $^{134}\text{Cs} \sim 10 \text{ Bq m}^{-3}$ ,  $^{137}\text{Cs} \sim 12 \text{ Bq m}^{-3}$ ) at  $41^\circ$ - $43^\circ\text{N}$  lies at 30-220  
10 m where mode waters formed through deep winter mixing in 2011 outcropped in the western North  
11 Pacific. The strongest 2015  $152^\circ\text{W}$  Fukushima-source radiocesium signal is associated with  
12 Dense-Central Mode Waters consistent with the densest variety of these mode waters being formed  
13 off the coast of Japan 4 years earlier. The radionuclide signal transited the basin along subsurface  
14 mode water isopycnals mainly on the northern side of the subtropical gyre before outcropping at  
15 and to the east of the  $152^\circ\text{W}$  line. In 2015, the densest  $152^\circ\text{W}$  waters with  $^{134}\text{Cs}$  lie at  $\sim 435$  m in  
16 the bottom range of Dense-Central Mode Water at  $40^\circ\text{N}$ . There is a weak, but detectable, signal in  
17 the boundary current off both Kodiak and Sitka. The deepest detectable  $^{137}\text{Cs}$  (weapon's testing  
18 background) are found at and to the north of  $45^\circ\text{N}$  at 900–1000 m. With the exception of a single  
19 subsurface sample near Hawaii, as of spring 2015, the southernmost  $^{134}\text{Cs}$  was found above 200 m  
20 at  $30^\circ\text{N}$ . A total date-corrected  $^{134}\text{Cs}$  inventory of 11-16 PBq is estimated. Qualitative comparison  
21 to model output suggests good consistency in terms of general location, latitudinal breadth, and  
22 predicted depth of penetration, allowing discussion of the bigger picture. However, the model's  
23 2015  $152^\circ\text{W}$  radiocesium signal is quantitatively weaker and the core is offset in latitude,  
24 potentially due to the lack of consideration of atmospheric deposition.

## 25 **Keywords**

26 Fukushima radiocesium

27 Mode water

28 North Pacific

29 Radionuclide Tracer

30 Ocean Circulation

## 31 **1. Introduction**

32 In the Northwest Pacific, warm tropical/subtropical waters meet cold, upwelled, nutrient rich  
33 waters from the north in a confluence zone east of Japan. Here, a variety of mode waters are formed  
34 in deep winter mixed layers, reaching 300-400 m. It is also here that the radionuclide  
35 contamination from the 2011 Fukushima Dai-ichi Nuclear Power Plant (FDNPP) accident was  
36 directly discharged into the ocean and where the major portion of the atmospheric deposition was  
37 thought to have occurred. This study examines the spread of Northwest Pacific mode water (MW)  
38 from the perspective of observations made 4 years after the accident along 152°W and in the  
39 Alaska Gyre. While many different radioisotopes were released as a result of the 2011 accident,  
40 we focus on radiocesium (henceforth referred to as Cs), in particular  $^{137}\text{Cs}$  (30.07-year half-life)  
41 and  $^{134}\text{Cs}$  (2.06-year half-life). Although the Pacific Ocean has received Cs input in the past, most  
42 notably due to nuclear weapons testing during the 1950's and 60's, given its two-year half-life, the  
43 presence of  $^{134}\text{Cs}$  is a unique diagnostic tool for indicating the presence of waters derived from the  
44 FDNPP. Henceforth, water tagged with  $^{134}\text{Cs}$  will be referred to as FDNPP Cs or simply  $\text{Cs}_F$ . The  
45  $\text{Cs}_F$  release afforded an opportunity to employ a powerful, soluble, readily detectable tracer input  
46 to the ocean at a known time and location to better understand the timing and spread of North  
47 Pacific MW.

48 Section 1 includes a review of North Pacific circulation and mode waters, and a short history of  
49 North Pacific Cs. Section 2 presents the Northeast Pacific observed Cs dataset and its distribution.  
50 Section 3 relates the observed Cs patterns with MW distributions, calculates inventories, brings  
51  $^{90}\text{Sr}$  estimates to bear and compares the observations to model predictions. Section 4 is a summary.  
52 Throughout, radionuclide units are given as activity in Bq (1 Bq = 1 nucleus decay per  
53 second) and activity concentration  $\text{Bq m}^{-3}$ .

54 **1.1 North Pacific Circulation and Mode Waters** North Pacific surface circulation is composed  
55 of three wind driven gyres: one subtropical and two semi-distinct subpolar, the Alaska and Western  
56 Sub-arctic Gyres (Fig. 1). The western boundary Kuroshio Current separates from the coast at  
57  $\sim 35^\circ\text{N}$  as it turns into the open ocean. Bifurcating, the main portion flows east as a strong inertial  
58 jet known as the Kuroshio Extension (KE), and slightly further north, influenced by Oyashio  
59 waters, the Kuroshio Bifurcation Front (KBF) extends eastward to become the Subarctic Current  
60 (Oka and Qiu, 2012).

61 In the west, to the south of the frontal regions (KE Front, KBF and further north near the Subarctic  
 62 Front) strong heat loss to the atmosphere results in vertical convective mixing in winter. These  
 63 regions of deep mixing have been illustrated by February mixed layer depths (MLD) observed by  
 64 historical hydrography (Talley, 1988; Suga et al., 2004), satellites (e.g. Fig. 1) and profiling floats  
 65 (e.g. Whalen et al., (2012); Yoshida et al. (2015)). The resulting ventilated, low potential vorticity  
 66 “mode” waters that lie slightly above or within the permanent pycnocline are classified into six  
 67 classes according to their distinct but homogeneous hydrodynamical characteristics (Table 1) and  
 68 are reviewed in detail by Oka and Qiu (2012).

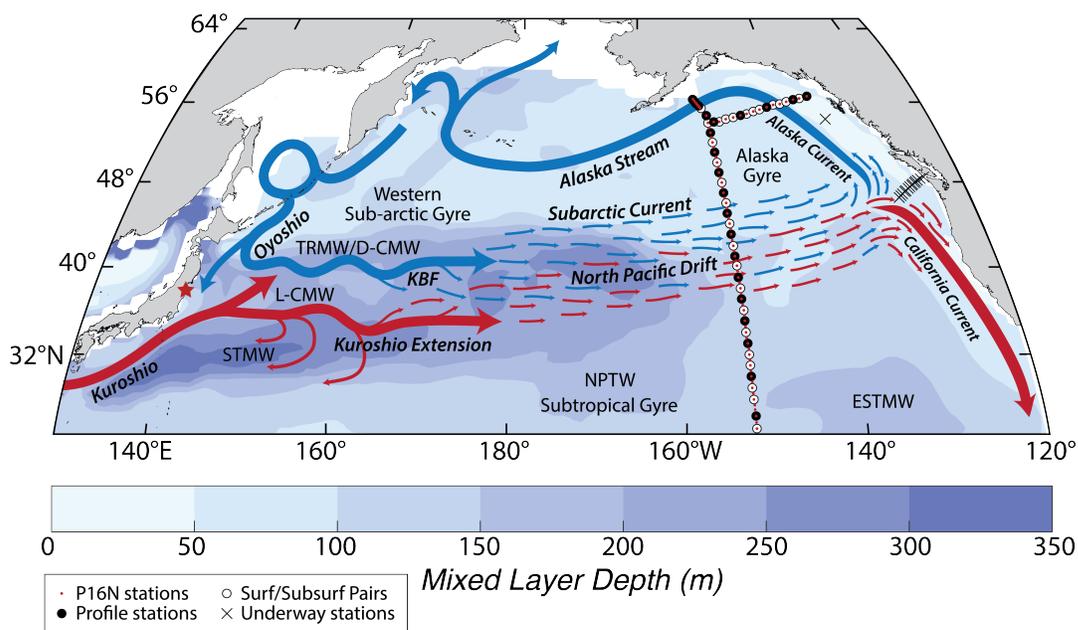


**Figure 1:** Schematic of North Pacific circulation overlaid on mean March mixed layer depth (blue shading, from GODAS, 2015; units: m) for the period 2011-2015. Line thickness does not represent current strength. Major currents, gyres and specific waters mass formation regions mentioned in the text are labeled: Kuroshio Bifurcation Front (KBF), Subtropical Mode Water (STMW), Light Central Mode Water (L-CMW), Dense Central Mode Water (D-CMW), Transition Region Mode Water (TRMW), Eastern Subtropical Mode Water (ESTMW) and North Pacific Tropical Water (NPTW). Hydrographic station locations for the northern end of the 2015 P16N/leg 2 occupation are shown as red dots. Black symbols indicate the location of cesium samples: open circle = subsurface/surface pair, filled circle = profile, and cross = underway surface sample. All P16N cesium stations are shown in Figure S1. The red star is FDNPP location.

69 *North Pacific Subtropical Mode Water* ( $24.5 < \sigma_0 < 25.9$ ) is formed to the south of the  
 70 KE front, and is associated with deep mixed layers (up to 400-450 m) and the anticyclonic  
 71 recirculation of the Kuroshio Current system (e.g.Suga and Hanawa, 1995, Qiu et al., 2006).  
 72 STMW’s low potential vorticity is thought to arise largely through lateral induction (i.e. advection

73 across a changing MLD) supported by the strong mixed layer front found on the southern flank of  
 74 the formation region, which is characterized by large surface density gradients (Suga et al. 2004).

**Table 1:** North Pacific Mode Water temperature, salinity and density characteristic definitions used for this study. TRMW definition comes from Saito et al. (2011). All others come from Bingham and Suga (2006) and references therein.

<b>Mode Water Name</b>	<b>Temperature Range (°C)</b>	<b>Salinity Range (g kg<sup>-1</sup>)</b>	<b>Density Anomaly (<math>\sigma_0</math>) (kg m<sup>-3</sup>)</b>
<b>NPTW</b>	20.0 – 24.0	34.9 – 35.5	23.6 – 25.1
<b>ESTMW</b>	16.0 – 22.0	34.6 – 35.4	23.9 – 26.1
<b>STMW</b>	15.4 – 19.7	34.6 – 35.0	24.5 – 25.9
<b>L-CMW</b>	12.0 – 14.5	34.3 – 34.6	25.5 – 26.3
<b>D-CMW</b>	6.0 – 10.0	33.7 – 34.2	25.9 – 26.9
<b>TRMW</b>	4.0 – 9.0	33.0 – 34.0	26.3 – 26.6

75 **Transition Region and Dense-Central Mode Waters** (TRMW  $26.3 < \sigma_0 < 26.6$ , D-CMW,  $25.9 <$   
 76  $\sigma_0 < 26.9$ ) are formed to the north of the KBF and to the south of the polar fronts as a zonal band  
 77 of deep winter mixed layers emanating from the west coast of Japan (39-43°N) and extending  
 78 beyond 160°W (Oka et al., 2011). Light Central Mode Water (L-CMW,  $25.5 < \sigma_0 < 26.3$ ) is formed  
 79 between the KE and the KBF in regions of moderate (150-225 m) mixed layers that do not change  
 80 significantly along isopycnals, where there is little diapycnal flow (Suga et al. 2004) and zonal  
 81 surface density gradients are small.

82 Central mode water (CMW) that is formed to the west of 170°E cannot be subducted into the  
 83 permanent pycnocline due to the deeper and lighter mixed layers found downstream. However,  
 84 CMW formed to the east of this longitude, where downstream winter mixed layers are shoaling,  
 85 can be, and therefore, can also be advected into the anticyclonic circulation of the subtropical gyre  
 86 (Oka et al., 2011). This picture is complicated by decadal-scale shifts in fronts and mesoscale eddy  
 87 activity linked to changes in surface wind forcing that can affect CMW formation (e.g. Oka and  
 88 Qiu, 2012 and references therein; Kawakami et al., 2016). The possible effects of CMW formation  
 89 variability include impacts on oxygen utilization rates (Kwon et al., 2016), carbon uptake and  
 90 storage rates, and sea-surface temperatures. While interannual variations (Kawakami et al., 2016)  
 91 and formation region eddy activity (Dong et al., 2017) are now being studied using Argo and  
 92 satellite records, less is understood about longer timescale variations and effects outside formation  
 93 regions.

94 **Eastern Subtropical Mode Water** (ESTMW  $23.9 < \sigma_0 < 26.1$ ) is by definition formed to the east  
95 of the dateline. While ESTMW forms in regions with fairly shallow MLDs (100-140 m, Katsura,  
96 2018), which are somewhat less homogeneous along isopycnals than those of CMW,  
97 compensating gradients in a fairly broad range of SSS and SST are responsible for minimal density  
98 gradients, so as for CMW, low potential vorticity is achieved through to lack of diapycnal flow  
99 (Suga et al., 2004).

100 **North Pacific Tropical Water** (NPTW  $23.6 < \sigma_0 < 25.1$ ), which is formed to the south of  $30^\circ\text{N}$  in  
101 the saline surface water Ekman convergence at the center of the subtropical gyre between  $15^\circ$ -  
102  $25^\circ\text{N}$ ,  $160^\circ\text{E}$ - $120^\circ\text{W}$  (Katsura et al, 2013) is also of interest because its  $30^\circ\text{N}$  limit may impact  
103 the farfield distribution of  $C_{\text{SF}}$ . While warmer and saltier than North Pacific MW, it partially  
104 overlaps ESTMW and STMW geographically as well as in density space.

105 A number of MW characteristic definitions exist in the literature (e.g. Hautula and Reommich,  
106 1998; Mecking and Warner, 2001; Oka and Suga, 2005; Qu et al., 2001; Oka et al., 2007, 2011,  
107 2015; Rainville et al., 2014; Katsura, 2018) some of which suggest narrower or slightly offset  
108 ranges. We use those described in Table 1. Across the broader Pacific, these waters have been  
109 recognized by their natural physical characteristics obtained at the time of formation. Here, we  
110 have the opportunity to use an anthropogenic tracer (i.e.  $C_{\text{SF}}$ ) that was unintentionally introduced  
111 to the ocean at a time and location that coincided with water mass formation.

## 112 **1.2 Radiocesium in the Pacific**

113 **History of Ocean Cs prior to FDNPP Release:** The largest input of cesium isotopes to the ocean  
114 is fallout from atmospheric nuclear weapons testing in the late 1950s and early 1960s, which was  
115 highest in mid-latitudes in the northern hemisphere (e.g. Aarkrog, 2003). Programs in the 1960s  
116 and 1970s began to measure the weapon's testing Cs ( $C_{\text{SWT}}$ ) oceanic distribution along with several  
117 other isotopes (e.g. tritium,  $^{14}\text{C}$ ,  $^{90}\text{Sr}$ , and Pu). Its soluble nature (e.g.  $<0.1\%$  of Cs is caught on a  
118 one-micron filter; Buesseler et al., 2012) allows Cs to be used as an ocean circulation tracer.

119 Additional  $^{137}\text{Cs}$  inputs to the ocean from reprocessing plants in Europe peaked in the 1970s, but  
120 did not impact Pacific waters. In 1986, Chernobyl became the largest accidental release of  $^{137}\text{Cs}$ .  
121 Although the total atmospheric release of radioisotopes from Chernobyl was about ten times that  
122 of FDNPP (Steinhauser et al., 2014), only a small fraction was deposited in the North Pacific.  
123 Therefore, the 15-20 PBq (e.g. Inomata et al., 2018; Aoyama et al., 2019) of input via atmosphere

124 and ocean from the 2011 FDNPP accident represents the largest accidental source of radioisotopes  
125 to this basin. It increased the existing 2011 North Pacific Cs inventory of 69 PBq (Aoyama et al.,  
126 2012) by 20-27% (Inomata et al., 2016; Aoyama et al 2016b, 2019).

127 With its short half-life,  $^{134}\text{Cs}$  uniquely “tags” water as being of Fukushima origin (i.e.  $\text{Cs}_{\text{SF}}$ ). The  
128 longer half-life of the  $^{137}\text{Cs}$  isotope means that the  $^{137}\text{Cs}$  signal that entered the surface ocean during  
129 nuclear weapons testing prior to the treaty signed in 1963 is still measurable today (Bowen et al.,  
130 1980; United Nations, 2000). More than half a century of ocean mixing and dispersion has lowered  
131 the concentrations of this weapons-based isotope ( $\text{Cs}_{\text{WT}}$ ) to background levels of 1.0–2.0  $\text{Bq m}^{-3}$   
132 (Aoyama and Hirose, 2008; Inomata et al., 2009; Aoyama et al., 2012). Due to the lack of deep  
133 water formation fallout delivery to the surface Pacific Ocean has tended to remain in the upper  
134 water column. How deeply the  $^{137}\text{Cs}$  has been mixed down over the last half century in the eastern  
135 North Pacific and the effects of this mixing on the uniformity of the  $\text{Cs}_{\text{WT}}$  background in the region  
136 will be discussed in Section 3.3.

137 ***FDNPP Radionuclide Release:*** The FDNPP, which includes six reactors, is located just north of  
138 the Kuroshio separation point on the northeast coast of Japan ( $37^{\circ}25'\text{N}$ ,  $142^{\circ}2'\text{E}$ , Fig. 1). In March  
139 2011, the offshore earthquake, and resulting tsunami and aftershocks caused a loss of power at the  
140 FDNPP. Soon thereafter, destabilization led to both a release of radioactive materials to the  
141 atmosphere (i.e. widespread atmospheric deposition – AD) through venting, hydrogen explosions  
142 and fire, and a leakage of coolant water through direct discharge into the ocean, i.e., the point-  
143 source direct ocean discharge – DOD – just off the FDNPP (Chino et al., 2011; Butler, 2011;  
144 NSCJ, 2011, Buesseler et al., 2017). Both AD and DOD had a  $^{134}\text{Cs}/^{137}\text{Cs}$  ratio of  $0.99\pm 0.03$   
145 (Buesseler et al., 2011). While no direct fallout observations over the oceans exist and total  
146 magnitudes are still subject to debate, transport models suggest that the bulk of the AD to the ocean  
147 occurred to the northeast of the plant (e.g. Stohl et al., 2012; Tsubono et al., 2016, Aoyama et al.,  
148 2016b) and that about three-quarters of the contamination that entered the atmosphere landed in  
149 the Northwest Pacific in near-shore waters (Buesseler et al., 2017; Inomata et al., 2018).

150 Injected from the shoreline, at its peak on 6 April 2011, the highest Cs activities measured in the  
151 ocean off the FDNPP were order  $68\times 10^6 \text{ Bq m}^{-3}$  (Buesseler et al., 2017 and others), representing  
152 more than a 10 million-fold increase over prior activities. Both observational evidence and  
153 numerical model simulations indicate relatively rapid (within a few months) advection of

154 contaminants eastward (Buesseler et al., 2012; Tsumune et al., 2012; Rypina et al., 2013) into the  
155 highly energetic mixed water region in the confluence of the Kuroshio and Oyashio (Fig. 1). Cs  
156 levels decreased rapidly in the months following the accident as maxima mixed vigorously and  
157 moved offshore carried by the strong and highly turbulent Kuroshio Current and KE (Rossi et al.  
158 2013). Although, 90% of the DOD occurred by 12 April, 2011, attesting to continued leakage,  
159 ocean Cs levels close to the FDNPP remained elevated –  $1000 \text{ Bq m}^{-3}$  (outflow  $\approx 10 \text{ GBq day}^{-1}$ )  
160 four years after the accident (Buesseler et al., 2011, 2017) and  $20 \text{ Bq m}^{-3}$  (outflow  $\approx 2 \text{ GBq day}^{-1}$ )  
161 seven years after (Kyodo News, 2018).

### 162 **1.3 Ocean Focused Investigations of FDNPP Radionuclides**

163 In 2011, the Japanese government (MEXT, 2011b) and the Tokyo Electric Power Company  
164 (TEPCO, 2011) monitored direct ocean discharge within 30 km of the coast. Near shore  
165 monitoring (to within 1 km of the power plant) continues to today (TEPCO, 2017; Kyodo News,  
166 2018). Repeat surveys have been undertaken in the western basin near Japan (e.g. Men et al., 2015,  
167 Kumamoto et al., 2014, 2017), but observations of the radionuclide activity in the open-ocean have  
168 been sporadic as opportunities have arisen. These observations include samples scattered across  
169 the basin (e.g. Aoyama et al., 2011, 2012, 2013, 2016a,b, 2019; Kamenik et al., 2013), and more  
170 recent samples obtained as ancillary measurements on transects (e.g. Yoshida et al., 2015;  
171 Kaeriyama et al., 2016; Kumamoto et al., 2016b) and in the eastern basin (Smith et al., 2015,  
172 2017), as well as samples provided by both members of the science community and the public  
173 along the U.S./Canadian shoreline (ORO, 2013). Surface drifters deployed near the FDNPP in  
174 early summer 2011 showed trajectories crossing the basin generally following the large-scale  
175 ocean circulation after one year (Rypina et al 2013). From June 2011 observations it was  
176 determined that long-lived isolated eddies and western boundary current dynamics were the  
177 dominant factors defining  $C_{SF}$  dispersion in the far western North Pacific on a 3-month time-scale  
178 (Rypina et al., 2013). As the contaminated water spread horizontally across the North Pacific basin,  
179 the modeling studies of Behrens et al. (2012) and Rossi et al. (2013) were among the first to report  
180 substantial vertical intrusion of Cs into the ocean interior, especially when the surface plume met  
181 late-winter/spring deep pycnostads in well-known MW formation regions.

182 Four meridional sections at  $147^\circ\text{E}$  (30 Oct. 2012 - 5 Nov. 2012),  $149^\circ\text{E}$  (20 Dec. 2011 - 9 Feb.  
183 2012),  $155^\circ\text{E}$  (25 Oct. 2012 - 29 Oct. 2012) and  $165^\circ\text{E}$  (10 Jun. - 16 Jul. 2012) provided early

184 observational evidence of entrainment, subduction and advection of  $^{134}\text{Cs}$  in MW to the north and  
185 south of the Kuroshio. About 9-months after the accident, observations at  $149^\circ\text{E}$  suggested that  
186 the bulk of the  $^{134}\text{Cs}$  passed through the transition region ( $35^\circ\text{-}40^\circ\text{N}$ ) between the surface and 200  
187 m ( $\sigma_\theta=26.4\text{-}26.8$ , maximum  $\sim 16\text{ Bq m}^{-3}$ ) (Kumamoto et al., 2014). By the fall of 2012, at  $147^\circ\text{E}$   
188 the signal remaining in the transition region was concentrated at  $38^\circ\text{-}40^\circ\text{N}$  ( $\sigma_\theta=26.1\text{-}26.4$ ,  
189 maximum  $\sim 14\text{ Bq m}^{-3}$ ) at 150 m (Kaeriyama et al., 2016, values decay corrected to Apr 6, 2011).  
190 At  $155^\circ\text{E}$ , the transition region signal had a similar maximum ( $\sim 15\text{ Bq m}^{-3}$  at  $38.5^\circ\text{N}$ ,  $\sigma_\theta=26.6$ ),  
191 but also a recognizable 100-300 core across from  $34^\circ\text{N}$  to  $40^\circ\text{N}$ . At  $36^\circ\text{-}38^\circ\text{N}$  there were secondary  
192 maxima ( $\sim 14\text{ Bq m}^{-3}$ ) at 400 m,  $\sigma_\theta=26.4$  that extended down to 500 m (Kaeriyama et al., 2016).

193 These meridional lines also saw the subduction, capping and spreading of STMW to the south of  
194 the KE. In January-February 2012, a subsurface  $^{134}\text{Cs}$  maximum ( $\sim 18\text{ Bq m}^{-3}$  at 400 m) at  $149^\circ\text{E}$ ,  
195  $34^\circ\text{N}$  was observed and this 300-400 m core, although attenuating southward, was detectable as  
196 far south as  $20^\circ\text{N}$  (Kumamoto et al., 2014). By the fall of 2012, the  $^{134}\text{Cs}$  core was observed at  
197 200-400 m at  $147^\circ\text{E}$ , throughout the  $30^\circ\text{-}35^\circ\text{N}$  region with maxima  $10\text{-}14\text{ Bq m}^{-3}$  in the  $24.6$  to  
198  $26.1\sigma_\theta$  range (Kaeriyama et al., 2016). These observations are consistent with those made a few  
199 months earlier at  $165^\circ\text{E}$ , which presented double  $^{134}\text{Cs}$  cores to the south and north of the KE ( at  
200  $\sim 30^\circ\text{N}/150\text{ m}$  and  $\sim 40^\circ\text{N}/300\text{ m}$ , respectively) in a pattern of detectable signal that spread from  
201  $\sim 23\text{-}46^\circ\text{N}$  (Aoyama, 2016a).

202 Yoshida et al. (2015) investigated the spread of  $\text{Cs}_\text{F}$  on a 2-year timescale utilizing the samples  
203 obtained from the variety of cruises including the 2013 P02 transect that crossed the basin at  $30^\circ\text{N}$ .  
204 They found that at this latitude the leading edge of the surface  $\text{Cs}_\text{F}$  signal had reached  $174^\circ\text{W}$  by  
205 the spring of 2012. A year later, with an average advection speed of  $5\text{ cm s}^{-1}$  it was observed at  
206  $160.6^\circ\text{W}$ . This rate of spread at  $30^\circ\text{N}$  agreed well with drifter and model estimates (Aoyama et al.  
207 2016a). Although the  $30^\circ\text{N}$  subsurface data set was sparse, it was found that two years after the  
208 accident the maximum  $\text{Cs}_\text{F}$  signal west of  $173.3^\circ\text{E}$  lay at  $\sim 300\text{ m}$ , but shoaled sharply to 200 m  
209 near the dateline and remained subsurface until the signal disappeared at  $160.6^\circ\text{W}$ .

210 At  $40^\circ\text{N}$ ,  $\text{Cs}_\text{F}$  had reached the dateline by July 2012 suggesting an average advection speed of  $8.5$   
211  $\text{cm s}^{-1}$ , which slowed to  $5\sim\text{cm s}^{-1}$  by the time the signal reached  $160^\circ$  to  $170^\circ\text{W}$  (Yoshida et al.,  
212 2015; Inomata et al., 2018). In the northeast, Cs levels were being monitored along Line-P (Fig.  
213 S1). Here, Smith et al., (2015) first detected  $^{137}\text{Cs}$  greater than the background (which they took to

214 be  $\sim 1 \text{ Bq m}^{-3}$ )  $\sim 1500 \text{ km}$  west of the Canadian coast in June 2012. A year later, order  $1 \text{ Bq m}^{-3}$   
215 values were observed on the Canadian Shelf and by early 2014,  $^{137}\text{Cs}$  values as high as  $2 \text{ Bq m}^{-3}$   
216 were observed throughout Line-P (Smith et al., 2017). These results were corroborated by 2014  
217 observations obtained between Dutch Harbor, AK and Eureka, WA, where a clear FDNPP surface  
218 signal with  $^{134}\text{Cs}$  values of  $2\text{-}4 \text{ Bq m}^{-3}$  was found in the Alaska Gyre along with one higher value  
219 ( $^{134}\text{Cs} = 5.4 \text{ Bq m}^{-3}$ ) off the coast WA (Yoshida et al., 2015).

220 Compiled surface  $^{137}\text{Cs}$  measurements obtained between July 2011 and December 2012 across a  
221 broad expanse of the North Pacific Ocean (Aoyama et al., 2016a) suggest that in the Northeast  
222 Pacific, after the first few months, the effects of Fukushima sourced AD could not be distinguished  
223 from the weapons testing background. This result is supported by the findings of Buesseler et al.,  
224 (2017) in their compilation of surface data  $^{137}\text{Cs}$  that extends to April 2016 (see their figure 2) and  
225 Kumamoto et al. (2016b) who concluded that the main bulk of the AD occurred in the Bering Sea  
226 and between  $25^\circ\text{N}$  and  $50^\circ\text{N}$  in the northwestern basin. So, while there was certainly some  
227 atmospheric delivery of  $\text{Cs}_F$  to the Northeast Pacific, the early lack of substantially elevated  $^{134}\text{Cs}$   
228 in the surface ocean to the east of the dateline suggests that  $\text{Cs}_F$  found at  $152^\circ\text{W}$  in the spring of  
229 2015, whether AD or DOD, was input to the ocean in the west and advected eastward. As the  
230  $^{134}\text{Cs}/^{137}\text{Cs}$  ratio in the AD and DOD were the same, the two are indistinguishable in our Cs data  
231 set. Therefore, we presume that the  $^{134}\text{Cs}$  signal observed in 2015 at  $152^\circ\text{W}$  is derived from a  
232 combination of the FDNPP DOD and AD that entered the ocean in the western basin. Likewise,  
233 we assume that patterns of  $^{137}\text{Cs}$  that mimic those of  $^{134}\text{Cs}$  are from an FDNPP source (we will  
234 come back to this in Section 3.3).

235 Here, we present the 2015 distribution of  $\text{Cs}_F$  in the Northeast Pacific along  $152^\circ\text{W}$ . Using these  
236 observations, we seek to elucidate the history of mode waters that have traversed the basin over  
237 the previous 4 years.

## 238 **2. The 2015 Radionuclide Dataset, Chemical Analysis and Distribution**

### 239 **2.1 Sampling**

240 In the spring of 2015 (Table 2) 395 radionuclide samples were obtained from the GO-SHIP  
241 occupation of the  $152^\circ\text{W}$  line P16N (Figs. 1, S1) beginning with twenty 12-sample radionuclide-  
242 only casts each going from  $\sim 10 \text{ m}$  to  $\sim 1000 \text{ m}$ . Use of the underway seawater system on station

243 and efficient use of water remaining in the bottles after all other sampling had been completed on  
244 regular hydrographic casts produced another 155 samples.

245 These included surface samples obtained from the underway seawater system as the ship steamed  
246 from the outer boundary of the U.S. Exclusive Economic Zone (EEZ) into Seattle, a few short  
247 profiles in shallower waters coming up the slope toward Kodiak and Sitka, and about 50  
248 surface/subsurface pairs. This sampling scheme provided  $\sim 1^\circ$  spacing along  $152^\circ\text{W}$  and a more  
249 broadly spaced survey across the Alaska Gyre (Fig. 1, S1). The ‘cross-gyre’ transect began at  
250  $54.1^\circ\text{N}$ ,  $151.1^\circ\text{W}$ , 100 km east of the meridional line and with an average latitude of  $55.5^\circ\text{N}$   
251 followed a portion of the 1993 WOCE P17N survey track. Of the 395 samples taken, 292 were on  
252 the  $152^\circ\text{W}$  line, 86 were on the cross-gyre transect, 15 were underway samples in the U.S. EEZ,  
253 and 2 were lost due to technical difficulties reducing the final number to 393.

**Table 2:** Start and end times and locations of the 2015 P16N radiocesium sampling.

<b>Component</b>	<b>Start Location</b>	<b>End Location</b>	<b>Month/Day Start</b>	<b>Month/Day End</b>
<b>Leg 1</b>	3.1°N, 152.0°W	21.5°N, 152.0°W	4/29/2015	5/11/2015
<b>Leg 2</b>	22.5°N, 152.0°W	56.4°N, 152.0°W	5/27/2015	6/18/2015
<b>Cross-Gyre</b>	54.1°N, 151.1°W	56.8°N, 136.0°W	6/19/2015	6/23/2015
<b>Underway</b>	54.3°N, 134.9°W	48.5°N, 124.8°W	6/24/2015	6/27/2016

## 254 2.2 Chemical Analysis

255 Here we present results from three radioisotopes:  $^{134}\text{Cs}$ ,  $^{137}\text{Cs}$ , and briefly  $^{90}\text{Sr}$  (half-life = 28.90  
256 years). Approximately 20 L seawater samples were collected into cubitainers via CTD rosette for  
257  $^{137}\text{Cs}$ ,  $^{134}\text{Cs}$  and  $^{90}\text{Sr}$  analyses. The samples were analyzed onshore at the Buesseler Laboratory at  
258 Woods Hole Oceanographic Institution using an ion-exchange resin-based method– potassium-  
259 nickel hexacyanoferrate (II) (KNiFC-Pan) (Šebasta 1997; Breier et al., 2016) for  $\gamma$ -counting on  
260 high-purity germanium well-type detectors for an average counting time of 50 hours.

261 Measurement errors include propagated recovery error (average  $2.0\pm 0.0\%$ ) and detector count  
262 error (varies by sample). The average recovery was  $98.5\%\pm 1.7\%$  with a range of 81%-100% and  
263 a median 99.0%. Decay correction  $^{134}\text{Cs}$  ( $^{137}\text{Cs}$ ) measurement error ranged from 0.02 to 1.30 (0.01  
264 to 0.60)  $\text{Bq m}^{-3}$ . Determined at the time of measurement, the average detection limits for both  $^{134}\text{Cs}$   
265 and  $^{137}\text{Cs}$  are  $0.1 \text{ Bq m}^{-3}$  for Buesseler Laboratory measurements (Pike et al., 2012) and  $0.03 \text{ Bq}$

266 m<sup>-3</sup> for the few low count samples that were sent to the HADES Laboratory (HADES, 2020). For  
267 example, the deep 650 dbar <sup>134</sup>Cs at 35°N (0.04±0.02 Bq m<sup>-3</sup>) was measured underground at  
268 HADES. Of samples sent to the underground lab, WHOI (HADES) found detectable <sup>137</sup>Cs in 43  
269 (71) and detectable <sup>134</sup>Cs in 1 (25). No samples south of 30°N were measured at HADES. Note,  
270 no samples south of 30°N were measured at HADES. Henceforth, the term *significant* implies that  
271 a measurement is both greater than the detection limit and the estimated decay-corrected  
272 measurement error.

273 Samples were analyzed for <sup>90</sup>Sr in the Buesseler Laboratory via beta counting of its daughter  
274 product <sup>90</sup>Y (half-life = 64.1 hours) by a method adapted from Tazoe et al. (2017). Fe hydroxide  
275 co-precipitated samples were filtered through a 25 mm QMA filter, dried, and fixed onto beta  
276 mounts that were counted on Risø beta detectors (Risø National Lab; Roskilde, Denmark). The  
277 detection limit ranged from 0.2 – 0.4 Bq·m<sup>-3</sup> for an approximately 90 hour counting time. Aliquots  
278 were taken before and after adsorption for stable <sup>137</sup>Cs, <sup>134</sup>Cs, <sup>90</sup>Sr, and <sup>90</sup>Y to determine extraction  
279 recovery via inductively coupled plasma mass spectrometer (Thermo iCAP Qc). All results  
280 reported here, unless otherwise noted, are based on concentration decay corrected to the major  
281 liquid discharge event date of 6 April 2011 (Buesseler et al., 2011). All sampling locations and the  
282 associated Cs activities have been submitted to the US Global Ocean Carbon and Repeat  
283 Hydrography Program (CCHDO, 2019) and the IAEA MARIS database (MARIS, 2019).

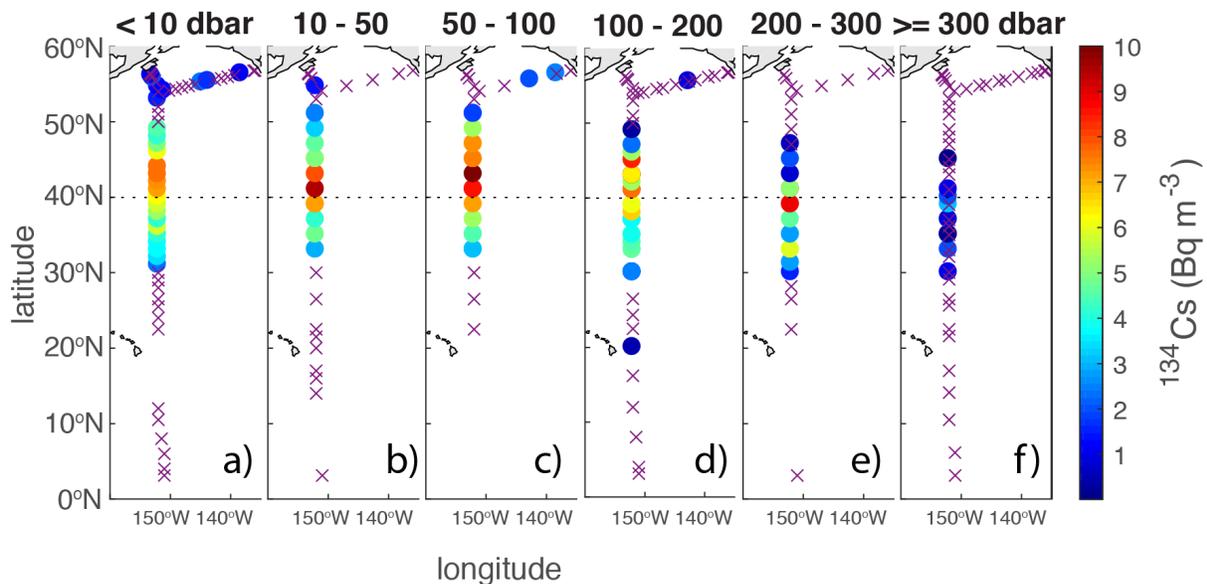
### 284 **2.3 The 2015 Northeast Pacific Radionuclide Distribution**

285 On P16N, C<sub>SF</sub> is evident from 30°N to the coast of Alaska (Fig. 2). Of the 393 Cs samples, 123  
286 (31%) have significant <sup>134</sup>Cs activities (i.e. above the detection limit and greater than their  
287 measurement error). As expected, due to the existence of the C<sub>SWT</sub> background, a larger number  
288 372 (95%) had significant <sup>137</sup>Cs. Of the 82 surface <sup>134</sup>Cs samples (Fig. 2a), 37 (45%) have  
289 significant activities. There are marked southern and northern boundaries to the surface signal at  
290 30°N and 49°N. Significant subsurface activities are apparent on the approach up the northern  
291 slope (within the Alaska Stream) and scattered across the Alaska Gyre including in the path of the  
292 Alaska Current. We return to the cross-gyre leg in the next subsection and here focus on the 292  
293 152°W samples.

#### 294 ***Radiocesium distribution along the 152°W Meridian:***

295 Along 152°W with 106 (36%) of the  $^{134}\text{Cs}$  samples having significant activities. 278 (95%) of the  
 296 152°W samples had significant  $^{137}\text{Cs}$  signals (Fig. S2). Of the 186 samples with  $^{134}\text{Cs}$  below the  
 297 detection limit, 172 had detectable  $^{137}\text{Cs}$ .

298 The minimum significant 152°W surface  $^{134}\text{Cs}$  is  $0.04 \pm 0.02 \text{ Bq m}^{-3}$ . The five largest surface values  
 299 ( $> 7.0 \text{ Bq m}^{-3}$ ) lie along 152°W between 41°N and 44°N. The next highest ( $6.1 \pm 0.6 \text{ Bq m}^{-3}$ ) is  
 300 longitudinally contiguous at 40°N. Deeper in the water column (Fig. 2b-f) the greatest activities  
 301 are slightly more spread between about 39°N and 45°N. The highest  $^{134}\text{Cs}$  activity ( $10.3 \pm 0.8 \text{ Bq m}^{-3}$ )  
 302  $\text{m}^{-3}$ ) is found at 50-100 dbar at 43°N (Fig. 2c). At 30°N all  $^{134}\text{Cs}$  values are  $\geq 1 \text{ Bq m}^{-3}$ . The  
 303 southernmost significant  $^{134}\text{Cs}$  measurement, which is also subsurface (140 dbar), appears as an



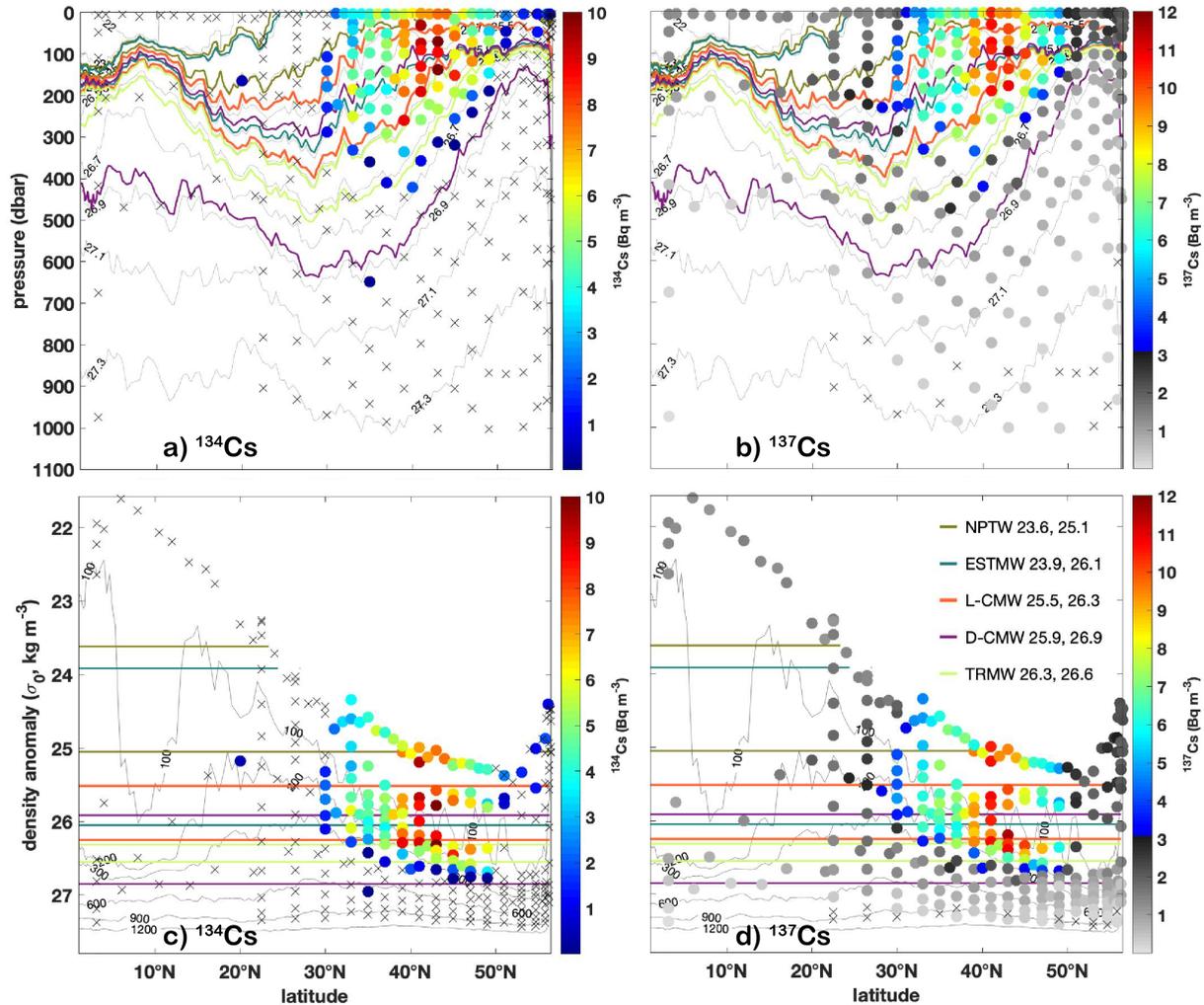
304 outlier ( $0.4 \pm 0.1 \text{ Bq m}^{-3}$ ) above the detection limit at 20°N as no other is found south of 30°N at  
 305 any depth (Fig. 2). Not so for  $^{137}\text{Cs}$ . Detectable  $^{137}\text{Cs}$  (Fig. S2) is found throughout the section  
 306 from the southernmost profile at 3°N to the Alaska Shelf. The only break is between 12° and 22°N  
 307 where there are no samples in the shallowest bin. The southern boundary of the  $^{134}\text{Cs}$  signal tends  
 308 northward with depth, a pattern made clearer by a latitude/pressure section plot (Fig. 3).

309 North of  $\sim 36^\circ\text{N}$ , both the maximum value in each profile and the deepest detectable signals shoal  
310 to the north. The  $C_{\text{SF}}$  follows the shoaling of the isopycnals northward. The abrupt boundary at  
311  $30^\circ\text{N}$  is clear in the  $^{134}\text{Cs}$  sections.

312 The  $^{137}\text{Cs}$  signal confirms the  $^{134}\text{Cs}$  findings (Fig. 3b, d) with maximum activities in similar  
313 geographic, depth and density spaces. Note, that although the signal is weak, the southern  
314 boundary is less abrupt giving the impression that the measurement at  $20^\circ\text{N}$  (that appeared as an  
315 outlier in the  $^{134}\text{Cs}$  distribution) is the southernmost extension of the deepest signal shoaling to the  
316 south. Whether or not this signal is following isopycnals will be discussed in the analysis of the  
317 circulation and local  $C_{\text{SWT}}$  background (Section 3.3).

318 A  $^{134}\text{Cs}$  section (Fig. 3a, c) highlights the subsurface and compact nature of  $C_{\text{SF}}$  at  $152^\circ\text{W}$ . The  
319 two largest activities, those greater than  $10 \text{ Bq m}^{-3}$ , are both found at  $43^\circ\text{N}$ . The 10 largest values  
320 are confined between  $25.2$  and  $26.5\sigma_0$ , all MW densities. Even the outlier at  $20^\circ\text{N}$  and the deepest  
321 detectable signal (at 645 dbar) still lie with MW density bounds as defined in Table 1.

**Figure 2:** Geographic distribution of detectable P16N  $^{134}\text{Cs}$  in pressure bins, shallow/left to deep/right: a) 0-10 dbar; b) 10-50 dbar; c) 50-100 dbar; d) 100-200 dbar; e) 200-300 dbar; and f) below 300 dbar. Upper surface pressure boundaries are inclusive. Colors indicate magnitude of activity decay corrected to April 6, 2011. Color bar is saturated at  $10 \text{ Bq m}^{-3}$ . Higher activities are plotted over lower activities, so be aware that deeper samples may overlay shallower samples. Values below the detection limit are shown by 'x' (see text). Fig. S2 is the equivalent for  $^{137}\text{Cs}$ .



322

**Figure 3:** a)  $^{134}\text{Cs}$  along  $152^\circ\text{W}$  in latitude-pressure space. Colors indicate magnitude of activity decay corrected to April 6, 2011. Color bar is saturated at  $10 \text{ Bq m}^{-3}$ . Gray x symbols are values below detection limit; gray lines are potential density anomaly relative to 0 dbar; colored lines are boundaries for each Table 1 water mass according to the legend in (d); b) Same as (a) for  $^{137}\text{Cs}$ . Color bar saturated at  $12 \text{ Bq m}^{-3}$ ; c) same as (a) in latitude- $\sigma_0$  space with gray curves representing pressure contours; d) Same as (c) for  $^{137}\text{Cs}$ . Note,  $^{137}\text{Cs}$  gray scale below  $3 \text{ Bq m}^{-3}$ . This value has been chosen to facilitate comparison to the  $^{134}\text{Cs}$  figure and to improve the representation of weaker signals. Although it is representative of the maximum remaining  $\text{Cs}_{\text{WT}}$  in the region, it should not be taken as a hard and fast estimate as  $\text{Cs}_{\text{WT}}$  has a latitudinal dependence (see Section 3.3).

323

324 **Radiocesium distribution on the zonal transect crossing the Alaska Gyre:** As noted earlier, some  
 325 low, but significant,  $^{134}\text{Cs}$  values were observed across the gyre (Fig. 2). At first glance the mainly  
 326 surface signal seems best described as spots of activity; in the east, interior to the slope approaching  
 327 Sitka, in the west near  $152^\circ\text{W}$ , and in the center of the gyre. The latter two and especially the  
 328 central gyre signal reached deeper into the water column, but still only to  $\sim 140$  dbar (Fig. 2c-d).

329 As on the meridional line, the maximum  $^{134}\text{Cs}$  activity ( $2.5 \pm 0.4 \text{ Bq m}^{-3}$ ) lies subsurface (80 dbar  
330 at  $138.3^\circ\text{W}$ ,  $56.4^\circ\text{N}$ ). The section plot (Fig. 4a) provides some further insight as it suggests that  
331 the  $^{134}\text{Cs}$  signal is mainly located above the pycnocline. The exception is the profile taken in the  
332 steeply sloping isopycnals at  $149^\circ\text{W}$  where  $^{134}\text{Cs}$  has been subducted locally in the front or has  
333 arrived at this location in the denser waters (e.g. perhaps TRMWs/D-CMWs outlined by light  
334 green/purple contours) of the boundary current. Whichever the case,  $\text{Cs}_\text{F}$  is being advected around  
335 the gyre in the boundary current which, according to both the density field in Fig. 4 and the P16N  
336 Lowered Acoustic Doppler Current Profiler (LADCP) direct velocity measurements is lying  
337 offshore of the easternmost stations.

338 The  $^{137}\text{Cs}$  cross-gyre maximum ( $3.8 \pm 0.2 \text{ Bq m}^{-3}$  found at the surface at  $144.8^\circ\text{W}$ ,  $55.2^\circ\text{N}$ ) was  
339 not co-located with the  $^{134}\text{Cs}$  maximum (which had an associated  $^{137}\text{Cs}$  of  $3.1 \text{ Bq m}^{-3}$ ).  
340 Nevertheless, the pattern of  $^{137}\text{Cs}$  (Fig. 4b) is similar and fills in some of the gaps left by the  $^{134}\text{Cs}$   
341 measurements in the near surface. All  $^{137}\text{Cs}$  with activity greater than the canonical background of  
342  $1\text{--}2 \text{ Bq m}^{-3}$  were found shallower than the upper boundary of L-CMW ( $25.5 \sigma_0$ , orange curve).  
343 Note also that Fig. 4 only shows the samples going down to 300 dbar. The deepest detectable cross-  
344 gyre  $^{137}\text{Cs}$  was found at 1000 dbar at the longitude of the deepest  $^{134}\text{Cs}$  value ( $142.5^\circ\text{W}$ , Fig. S3).  
345 However,  $^{137}\text{Cs}$  was not detected everywhere along the gyre section below 500 dbar. To the west,  
346 toward  $152^\circ\text{W}$  and away from the central portion of the cross-gyre transect, the  $^{137}\text{Cs}$  signal shoals.  
347 At the westernmost cross-gyre profile ( $151.1^\circ\text{W}$ ) the deepest  $^{137}\text{Cs}$  signals lies at  $\sim 450$  dbar, well  
348 above the deepest cross-gyre signals at 1000 dbar.

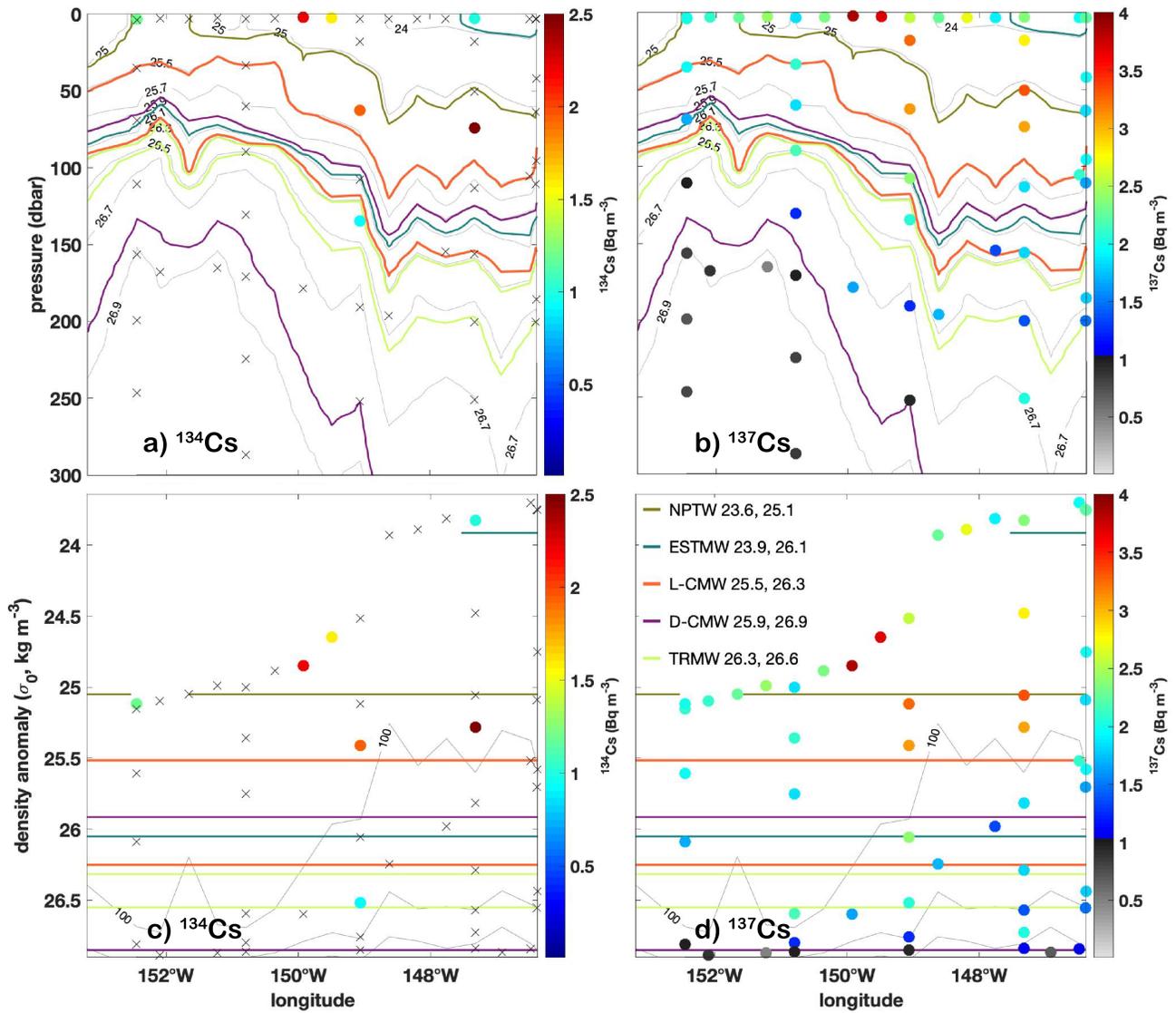


**Figure 4:** a) Significant  $^{134}\text{Cs}$  along the cross-gyre transect in longitude-pressure space. Colors indicate magnitude of activity decay corrected to April 6, 2011. Color bar is saturated at  $2.5 \text{ Bq m}^{-3}$ . Gray x symbols indicate values below detection limit; gray lines are potential density anomaly relative to 0 dbar; water mass density boundaries are indicated in color as in Figure 4; b) Same as (a) for  $^{137}\text{Cs}$ . Color bar saturated at  $4.0 \text{ Bq m}^{-3}$  and a change to gray scale occurs at  $1 \text{ Bq m}^{-3}$ . As for Fig. 3, gray scale does not represent  $C_{\text{WT}}$ , but is provided to improve the representation of weaker, but detectable  $^{137}\text{Cs}$  signals; c) Same as (a) in longitude- $\sigma_0$  space with gray curves representing 100, 200 and 300 dbar; d) Same as (c) for  $^{137}\text{Cs}$ . Note, that depths, densities and color bar are not the same as those in Fig. 3. Equivalent for  $^{137}\text{Cs}$  down to 1000 dbar is provided in the supplementary material (Fig. S3).

350 **Radiocesium distribution on underway leg into Seattle:** As in the cross-gyre samples, the  $^{134}\text{Cs}$   
 351 signal in the underway samples is not strong ( $< 2.5 \text{ Bq m}^{-3}$ ), but is significant (Fig. 5). The  
 352 observations indicate a stronger radionuclide signal associated with denser waters. The eastern  
 353 boundary along the North American west coast is well known as an upwelling system and here we  
 354 see that as surface waters become denser on the coastal approach,  $\text{Cs}_\text{F}$  traces the shoaling  
 355 isopycnals where they outcrop. The  $^{137}\text{Cs}$  observations (Fig. S4) support this result, though not  
 356 quite as clearly as they are clouded by variable and upwelling  $\text{Cs}_\text{WT}$ . Just to the north ( $48.5^\circ\text{-}50^\circ\text{N}$ ),  
 357 Line-P (Fig. S1) density sections based on observations show shoaling isopycnals – supporting the  
 358 idea of inshore upwelling within 500 km of the coast in this region and timeframe (see August  
 359 2015 panels of Smith et al. (2017) figure 2).

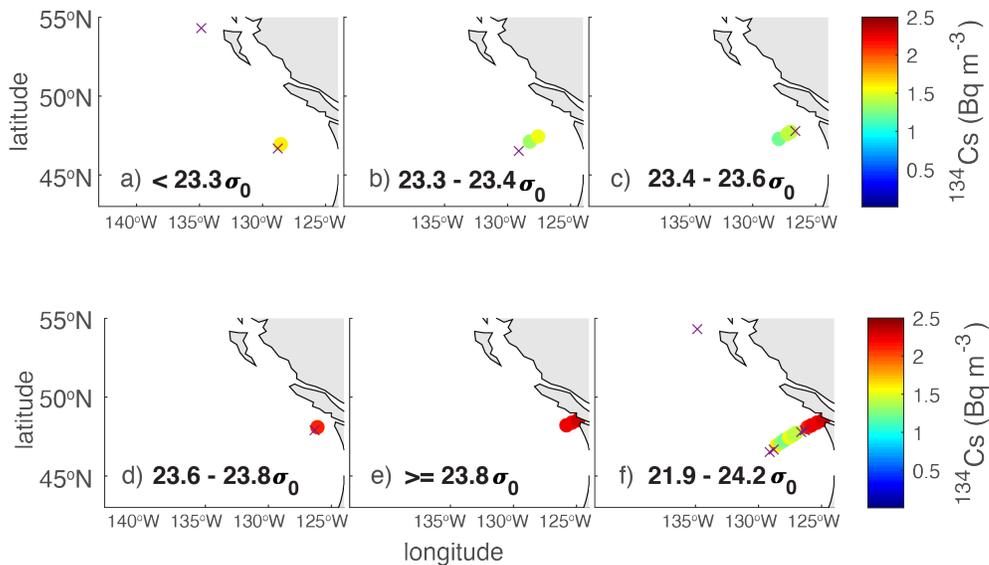


**Figure 5:** Surface  $^{134}\text{Cs}$  from underway samples in density anomaly bins. Densities are calculated from the ship's underway seawater system temperature and salinity sensor data (see explanation in the text). a) Density less than  $23.3 \sigma_0$ ; b)  $23.3\text{-}23.4 \sigma_0$ ; c)  $23.4\text{-}23.6 \sigma_0$ ; d)  $23.6\text{-}23.8 \sigma_0$ ; e) greater than  $23.8 \sigma_0$ ; and f) the full range  $21.9\text{-}24.2 \sigma_0$ . Upper surface density boundaries are inclusive. Colors indicate magnitude of activity decay corrected to April 6, 2011. Color bar is saturated at  $2.5 \text{ Bq m}^{-3}$ . Magenta x symbols indicate values less than the detection limit of  $0.1 \text{ Bq m}^{-3}$ . Equivalent figure for  $^{137}\text{Cs}$  is provided as supplementary Fig. S4. Equivalent figures in pressure space are not shown as these all surface measurements.

360 In summary, the P16N Cs sampling provides a May-June 2015 picture of  $\text{Cs}_\text{F}$  in the northeast  
 361 Pacific with the deepest significant  $^{134}\text{Cs}$  measurement at  $\sim 650$  dbar; the ten highest values  
 362 between  $39^\circ\text{N}\text{-}45^\circ\text{N}$  from just below the surface to 260 dbar; a maximum signal at  $43^\circ\text{N}$  (70 and  
 363 145 dbar); and an abrupt cutoff at  $30^\circ\text{N}$ . These observations in the east are consistent with earlier  
 364 findings in the west (e.g. Kumamoto et al., 2014; Kaeriyama et al., 2016) with a stronger signal

365 subsurface in the MW densities. In the eastern basin there is a shoaling of  $C_{SF}$  northward along  
366  $152^{\circ}W$  with the MW, an indication of the transport of a weak surface signal around the Alaska  
367 Gyre in the boundary current, and a stronger subsurface signal away from the coast at  $\sim 55^{\circ}N$ . The  
368 interior gyre presents a 1000 dbar deep bowl shaped  $^{137}Cs$  signal with the deepest values shoaling  
369 toward the coast to the east and to  $\sim 450$  m to the west at  $152^{\circ}W$ . Lastly, a pattern of upwelling  $C_{SF}$   
370 was found on the coastal approach into Seattle.

### 371 **3. Discussion**

372 The timing of maximum FDNPP AD and DOD introduced to the western North Pacific in late  
373 winter/early spring and the proximate North Pacific MW formation regions made it reasonable to  
374 assume from the beginning that  $C_{SF}$  would find its way into MW. As discussed earlier, many  
375 studies both observation- and model-based have borne this assumption out (e.g. Rossi et al., 2013;  
376 Kumamoto et al., 2014, 2017; Yoshida et al., 2015; Kaeriyama et al., 2016, Aoyama et al., 2016a;  
377 Kumamoto et al., 2017; Smith et al., 2017). Updating Kaeriyama et al. (2014), Kaeriyama et al.  
378 (2016) estimate that by the fall of 2012,  $4.2 \pm 1.1$  PBq  $C_{SF}$  had penetrated STMWs, leading Inomata  
379 et al. (2018) to conclude that  $2.5 \pm 0.9$  PBq  $C_{SF}$  had been injected into CMWs. While only 22% of  
380 the  $152^{\circ}W$  water column can be characterized as one or more of the MW according to all three  
381 Table 1 characteristics ( $\Theta$ ,  $S$ , and  $\sigma_0$ ) nearly 75% have potential densities in MW ranges, so we  
382 take the opportunity to determine the relative distribution and their water column  $C_{SF}$  inventory.

#### 383 **3.1 The Source of Mode Waters found at $152^{\circ}W$**

384 The L-CMW formation region lies directly in the path of the DOD between the fronts to the north  
385 and south (Fig. 1). However, in  $\Theta/S$  space (Fig. 6), while one of ten largest observed  $^{134}Cs$  activities  
386 (largest dots circled in black) is associated with L-CMW densities, nine of these ten as well as the  
387 deepest signals are associated with D-CMW, and in particular a regime where D-CMW  
388 characteristics overlap those of TRMW. Kumamoto et al. (2014) and Kaeriyama et al. (2016)  
389 reported that between  $147^{\circ}$ - $155^{\circ}E$  most of signal found in the 2012 transition region ( $35^{\circ}$ - $40^{\circ}N$ )  
390 was in “CMW”, but more precisely it was found in waters with TRMW/D-CMW densities.

391 ***MW in 2015 at  $152^{\circ}W$  and 2011-2015 MW Formation:*** To explain why we see  $C_{SF}$  so clearly in  
392 D-CMW and TRMW at  $152^{\circ}W$ , but far less so in L-CMW and STMW, we follow the work of  
393 Bingham and Suga (2006, henceforth BS06) to determine where and when these waters formed  
394 over the 2011-2015 timeframe and how they have been distributed since. BS06 compared the

395 extent of MW formation regions in 2006 based on Argo float data to the climatological average  
 396 formation regions suggested by the World Ocean Atlas 2001 historical hydrography (Conkright et  
 397 al., 2002). They reported that the overall distribution of suggested STMW formation sites in that  
 398 single year were similar to the climatological distribution. They also found that the denser CMW  
 399 formation regions were quite patchy and limited in 2006, and concluded that they varied more  
 400 spatially and temporally than those of STMW. BS06 did not look at TRMW because it was not  
 401 defined as a distinct MW until the following year (Saito et al., 2007, 2011).

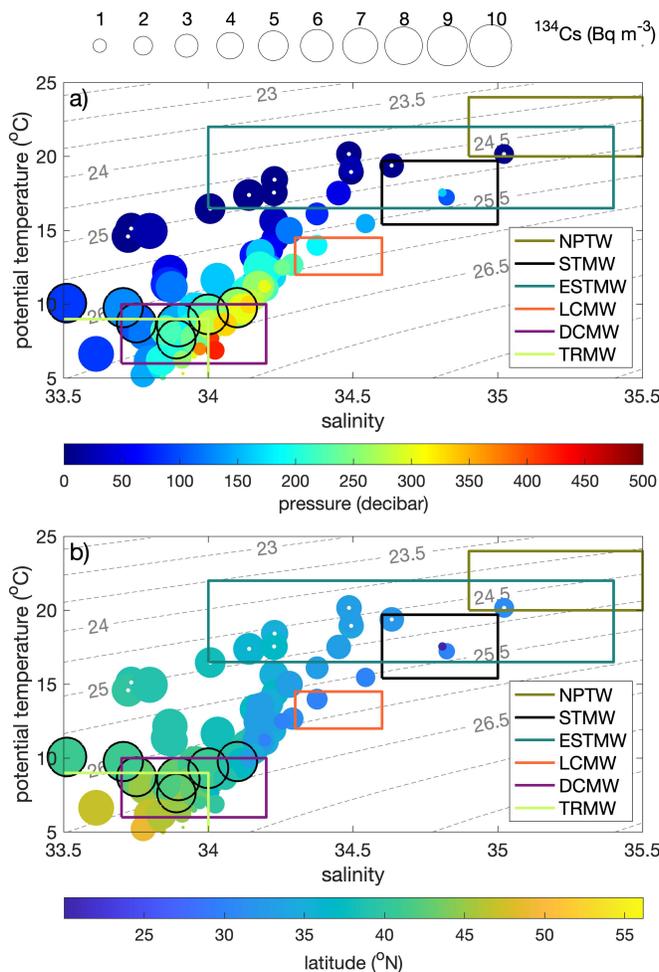


**Figure 6:** Potential temperature/salinity distribution of waters associated with  $^{134}\text{Cs}$  samples on the 152°W line. Size indicates magnitude of activity (scale provided at top of the figure). Surface (~5 m) samples have white dots in their centers. Ten largest values are outlined in black. Colored rectangles and contours outline the  $\Theta/S$  and  $\sigma_0$  space for each water mass as defined in Table 1, respectively. Colors match those used in Fig. 4. Circle colors indicate a) pressure and b) latitude associated with each sample. Equivalent figure for  $^{137}\text{Cs}$  is provided as supplementary Fig. S5.

402 Here, we employ some 113 thousand 2011-2015 Argo float profiles (Argo, 2019) to identify both  
 403 the formations sites and subsurface extent of North Pacific MW since the FDNPP accident.  
 404 Following BS06, we used the winter (January-March) MW properties at 10 dbar to identify  
 405 possible formation regions between 2011 and 2015 (Fig. 7, dark blue dots), noting that these can  
 406 also represent outcrops. We interpret locations with MW properties at 100 dbar but not at the

407 surface (Fig. 7, light blue dots) as capped MW formed at some recent point in time, not necessarily  
 408 2011-2015, and locations where those properties exist at both 10 dbar and 100 dbar (Fig. 7, pink  
 409 dots) as 2011-2015 MW formation.

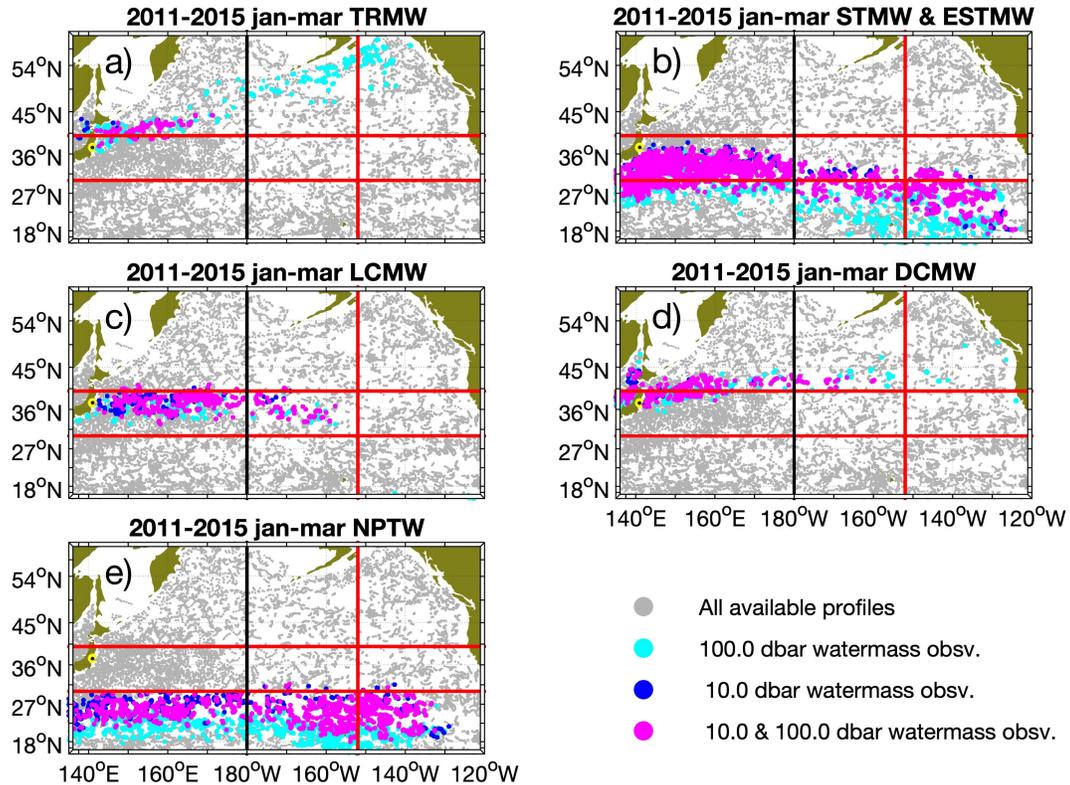


**Figure 7:** Locations of Argo profiles for the months of January-March between March 2011 and June 2015 (gray dots). Profiles with the temperature, salinity and density characteristics of a) TRMW, b) STMW west of the dateline and ESTMW east of the dateline, c) L-CMW, d) D-CMW and e) NPTW at 10 dbar (dark blue dots, i.e. possible formation sites), at 100 dbar (light blue dots, i.e. capped subsurface sites), and at both 10 dbar and 100 dbar (pink dots, i.e. formation sites). Water mass definitions are provided in Table 1. For reference: black line at 180° longitude, red lines at 30°N, 40°N and 152°W. Yellow circle with black dot on Japan coast indicates FDNPP.

410 The distribution of the Argo database MLDs (Fig. S6, based on Holte et al., (2017)) generally  
 411 agrees with the combined distribution from all our Fig. 7 panels. However, it is not possible to  
 412 create a one to one comparison. For example, due to the deeper STMW, CMW and TRMW  
 413 formation region MLDs, NPTW formation is washed out in the Fig. S6 representation, as is the  
 414 westward extension of ESTMW formation (see Katsura (2018), his figure 7).

415 Focusing on the areas with MW properties in the upper water column during January-March  
 416 timeframe between 2011-2015 (Fig. 7 pink dots), it can be seen that while the north/south extent  
 417 of ESTMW (Fig. 7b) at the dateline was similar (27°-34°N), in 2011-2015 STMW formed in a

418 narrower band ( $27^{\circ}$ - $37^{\circ}$ N) than in either 2006 or the climatological past ( $20^{\circ}$ - $37^{\circ}$ N) (See BS06  
419 their figure 3). This difference highlights the large inter-annual variability in geographical  
420 delimitation and spatial extent exhibited by these MW formation regions. While such variability  
421 might be studied by treating the Argo database year-by-year, observational gaps hinder such  
422 analysis. In addition, our main period of interest (2011-2015) is temporally and spatially well  
423 represented by Argo, which give us confidence in our results. We therefore leave investigation of  
424 inter-annual variability to future research.

425 The combination of multiple years of data, averages out inter-annual variability, returning less  
426 patchy CMW formation sites (Fig. 7c-d) than the 2006 data alone. The patterns suggest the  $C_{SF}$   
427 could well have been mixed/remixed into different MWs in different years as it was advected  
428 through the various mid-basin formation regions. L-CMW has a geographical extent similar to the  
429 climatology while D-CMW extends further south in the far west ( $\sim 37^{\circ}$ - $44^{\circ}$ N for 2011-2015  
430 compared to  $40^{\circ}$ - $44^{\circ}$ N for the climatology), suggesting D-CMW formation directly off the coast  
431 from the FDNPP during the 4 years of interest. The model-based results of Cedarholm et al. (2019)  
432 support this suggestion, reporting that the densest varieties of MW (as dense as  $26.8\sigma_{\theta}$ ) were  
433 formed in 2011 in the transition region. TRMW formation sites (Fig. 7a) during the more recent  
434 time frame are limited to a relatively thin line ( $40^{\circ}$ - $43^{\circ}$ N) west of  $170^{\circ}$ E. To the south, possible  
435 NPTW formation sites span most of the basin, expanding in latitude toward the east, but remaining  
436 to the south of  $30^{\circ}$ N. This is consistent with the Nie et al. (2016) analysis of ECCO model output  
437 that determined that NPTW subducts within the  $20^{\circ}$ - $30^{\circ}$ N band along  $150^{\circ}$ E- $130^{\circ}$ W. Of all these  
438 suggested formation regions, only ESTMW and NPTW overlap with the  $152^{\circ}$ W line. They both  
439 do so to the south of  $30^{\circ}$ N, indicating MW found to the north would have to have been advected  
440 into the region.

441 While all MW formation regions in the western basin lie within close proximity of the FDNPP,  
442 the STMW region is blocked by the Kuroshio and KE fronts (e.g. Rypina et al., 2013).  
443 Nevertheless, results from the western basin suggest that  $C_{SF}$  contaminated waters have been  
444 subducted across the front (e.g. Kumamoto et al., 2014; Garraffo et al., 2014; Yoshida et al., 2015;  
445 Aoyama et al., 2019). These waters have entered the recirculation where STMW forms (e.g.  
446 Aoyama et al., 2019). Such southward crossing is expected to occur more easily further out in the  
447 basin where the current becomes more diffusive (Rypina et al. 2014), has indeed occurred (e.g.  
448 Yoshida et al., 2015; Cedarholm et al. 2019).

449 Looking deeper in the water column (Fig. 8) provides insight into where the various MWs exist  
 450 inside and outside their formation regions. All five of the water masses discussed overlap with the  
 451 152°W line at some location and depth in the subtropics or to the north (Figs. 7-8). From the  
 452 surface to 100 dbar, NPTW exists well south of 30°N, and it recedes southward with depth (Fig.  
 453 8e): a pattern that suggests that what little  $C_{SF}$  found to the south of 30°N may be associated with  
 454 NPTW. It is, however, also true that ESTMW (Figs. 7b, 8b) water properties exist in the same  
 455 region and with a much broader fingerprint at depth. Therefore, we are not in a position to say  
 456 whether the few  $C_{SF}$  observations found to the south of 30°N are the result of local mixing of AD  
 457 or trans-basin advection.

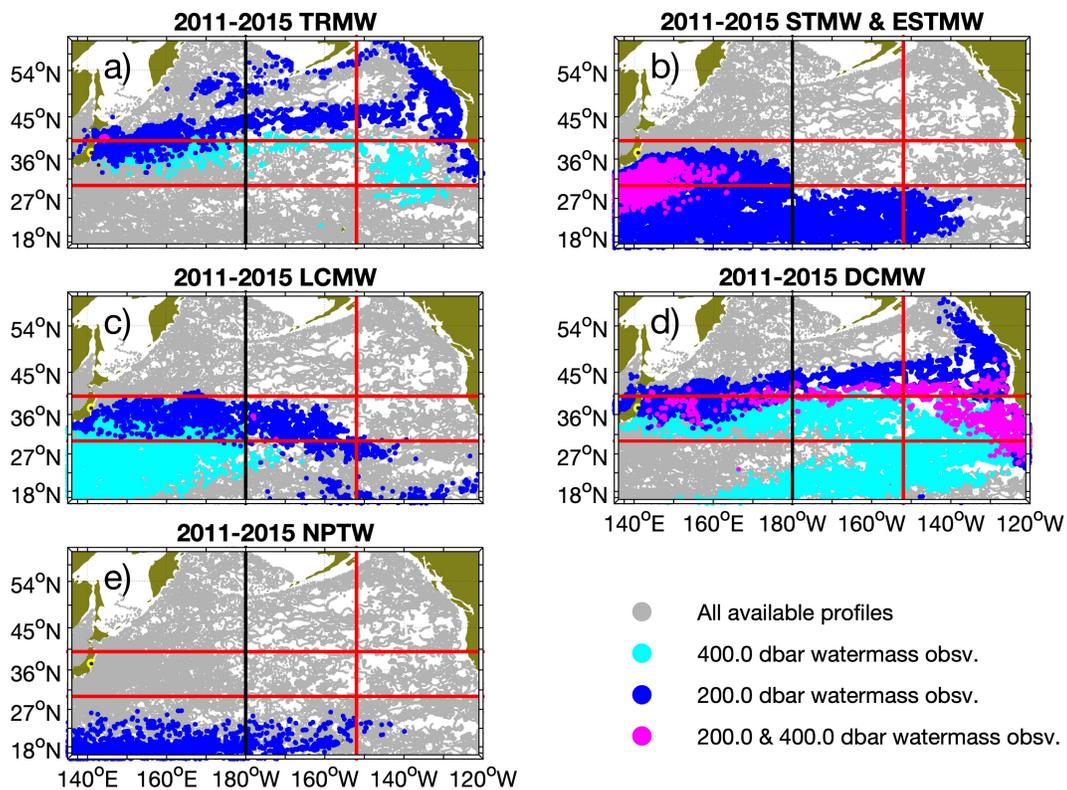


**Figure 8:** Same as Fig. 8 except showing all available Argo profiles between March 2011 and June 2015 (gray dots) with the specified water mass characteristics at 200 dbar (dark blue dots), 400 dbar (light blue dots), and both 200 dbar and 400 dbar (pink dots).

458 ***MW in 2015 at 152°W and Circulation:*** The previous discussion explains why we might expect  
 459 to see the strongest 152°W  $C_{SF}$  signal in D-CMW/TRMW, but does not necessarily explain the  
 460 weakness of the L-CMW signal (Fig. 6a). Upon exiting their respective formation regions, L-  
 461 CMW and D-CMW/TRMW are both advected eastward in the anticyclonic subtropical gyre

462 circulation. However, while the former does so predominantly on the southern (in)side of gyre, the  
463 latter takes the northern (out)side route. This suggests that L-CMW tagged with  $C_{SF}$  may have  
464 turned southward and eastward before arriving at  $152^{\circ}W$ . This pattern is consistent with the  
465 observations of  $^{137}C_{SWT}$  in L-CMW in the subtropical gyre further east at  $165^{\circ}E$  (e.g. Aoyama et  
466 al., 2008, their figure 3). Note, that at depth, subducted L-CMW may reach the  $152^{\circ}W$  (Fig. 8c),  
467 but only to the south of  $30^{\circ}N$  where no  $C_{SF}$  was found in 2015, i.e. timescales longer than 4-years  
468 may be necessary. Subsurface waters with D-CMW and TRMW properties extend to and beyond  
469  $152^{\circ}W$  (Fig. 8a, d). At 400 dbar, (Fig. 8, light blue dots) the pressure of our deepest non-outlying  
470  $C_{SF}$  signals (Fig. 3a), both TRMW and D-CMW cross  $152^{\circ}W$ , TRMW at and just south of  $40^{\circ}N$ ,  
471 and D-CMW in a broad region from  $\sim 43^{\circ}N$  to  $18^{\circ}N$ .

472 At these pressures, TRMW and D-CMW properties are found in a sweeping curve around the  
473 subtropical gyre – a signal not seen in the 2015  $C_{SF}$  observations, which are limited by the 4-year  
474 timescale. A similar timescale ( $\sim 3$ -5 years) is necessary for the core of the radionuclide plume to  
475 be simulated at about 500 m near  $150^{\circ}W/30^{\circ}N$  (Rossi et al. 2013, see their figure 4 and Section  
476 3.5). Water at both 200 dbar and 400 dbar (pink dots) at  $152^{\circ}W$  have D-CMW properties between  
477 about  $39^{\circ}$ - $43^{\circ}N$  and so spans of our maximum  $C_{SF}$  signal. At 200 dbar, D-CMW/TRMW  
478 properties overlap at  $\sim 45^{\circ}N$  and extend around the boundary of the gyre in the Alaska Current, but  
479 only TRMW properties are seen further west in the Alaska Stream. They are also seen at 100 dbar  
480 in this boundary current (Fig. 7a light blue dots). Both patterns suggest that near Sitka, the  
481 measured  $C_{SF}$  could be associated with upwelled versions of either of these water masses, but it is  
482 TRMW that has brought  $C_{SF}$  fully around the Alaska Gyre to where it was measured off the Alaska  
483 Shelf near Kodiak. This process is consistent with Line-P findings (Smith et al., 2017) and the  
484 Rossi et al. (2013) modeling study.

### 485 **3.2 $152^{\circ}W$ Radiocesium Inventories**

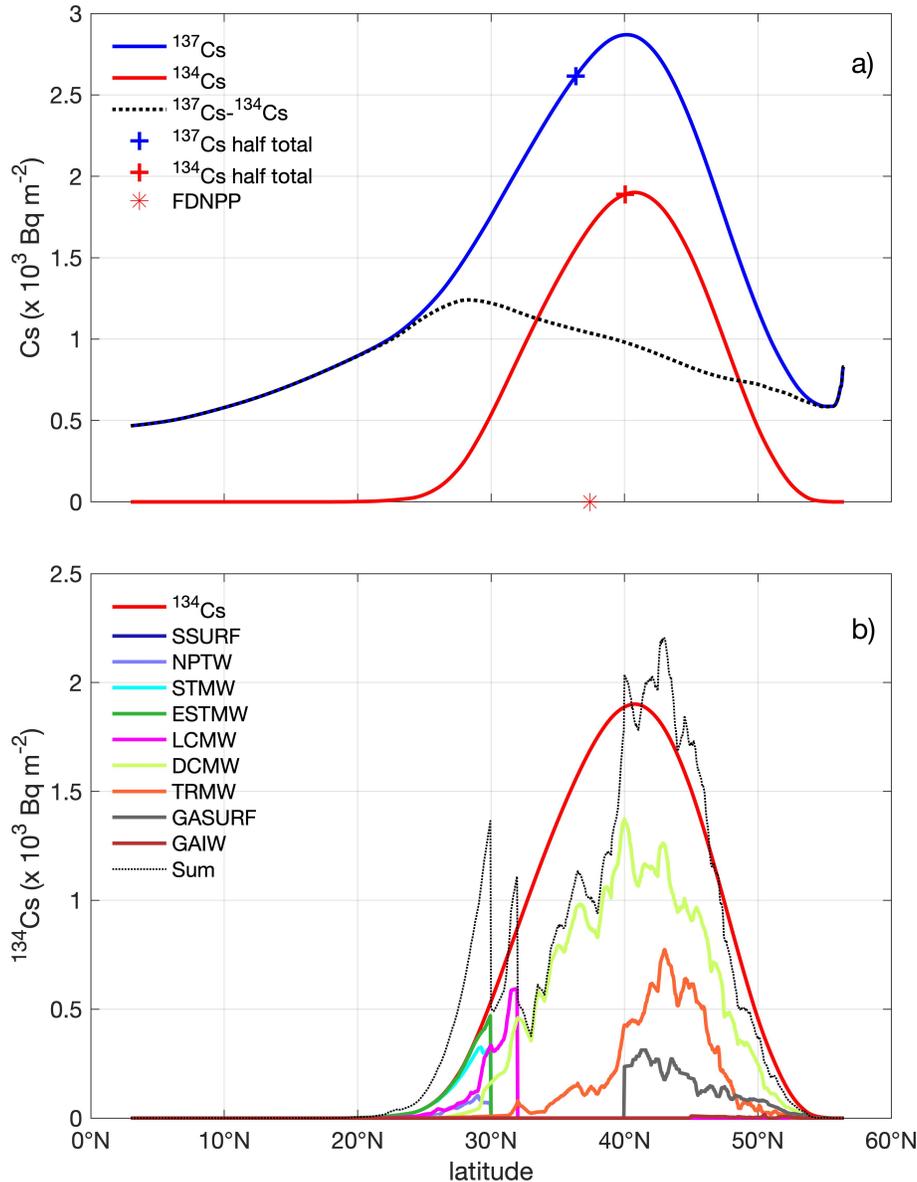
486 To obtain inventory estimates, water properties along  $152^{\circ}W$  were interpolated (but not  
487 extrapolated) onto a regular vertical (2 dbar) and meridional grid ( $0.05^{\circ}$  latitude) using a natural  
488 nearest neighbor interpolation. Given the relative lack of deep observations, all inventory  
489 calculations were performed between 0 and 700 m (a depth chosen to include our deepest  $^{134}Cs$   
490 signal). Integrating vertically (Fig. 9a) the maximum water column inventories of both  $^{137}Cs$  and  
491  $^{134}Cs$  are found at  $\sim 40^{\circ}N$  ( $2.9 \times 10^3$  Bq  $m^{-2}$  and  $1.9 \times 10^3$  Bq  $m^{-2}$  per meter of latitude, respectively).

492 Integrating along 152°W and assuming a 1 m width, we find local along-line (3.0°-56.45°N) water  
493 column inventories of  $8.3 \times 10^9$  Bq and  $3.2 \times 10^9$  Bq for  $^{137}\text{Cs}$  and  $^{134}\text{Cs}$ , respectively. The difference  
494 between these two inventories (Fig. 9a, dotted line) is our first rough estimate of the shape of the  
495 Cs background at 152°W. To determine the fraction of the  $\text{Cs}_F$  inventory in each of the water  
496 masses present in the region, we define three additional water masses so as to cover most of the  
497 water column above 700 m: (SSURF) surface water to the south of 30°N, defined as warmer,  
498 fresher and lighter than any in Table 1; (GASURF) Gulf of Alaska surface water defined to the  
499 north of 40°N and includes waters colder, fresher and lighter than those defined in Table 1; and  
500 (GAIW) Gulf of Alaska Intermediate Water, which spans a range of temperatures and salinities  
501 but in particular, is denser than  $26.9 \sigma_0$  (You, 2000; Kouketsu, 2007).

502 Quantifying what can already be generally seen in the pattern of isopycnal contours in Fig. 3, 44%  
503 of the 152°W water column can be associated with waters whose potential temperature ( $\theta$ ), salinity  
504 (S) and potential density anomaly ( $\sigma_0$ ) (rectangles in Fig. 6) lie in the range of one or more of the  
505 six water masses presented in Table 1 (plus SSURF, GASURF, and GAIW). If only density is  
506 used, 96% is captured, but there is so much overlap in definitions that comparison among  
507 contributions is not possible. Neither of these results is surprising given the number of Cs  
508 observations that do not overlap with the water mass rectangles outlined in Fig. 6 and the extreme  
509 overlap in density definitions found in Table 1. Therefore, we use  $\sigma_0$  along with the broad water  
510 mass latitudinal limits that were identified using the Argo profile data (Section 3.1), i.e. 30°N for  
511 subtropical and tropical waters and 32°N for L-CMW. With these criteria 74% of the 152°W water  
512 column is captured.

513 The  $^{134}\text{Cs}$  inventory to the south of 30°N (Fig. 9b) is unreliable as there are few Cs samples and  
514 only one detected  $^{134}\text{Cs}$  value. Further, while  $\theta/S$  are available south of 30°N, the overlap in density  
515 limits means there is little one can say about which water mass is responsible for bringing the one  
516 small Cs signal to the line other than the general conclusion that  $^{134}\text{Cs}$  is present in lighter  
517 subtropical waters. Between 30°N and 32°N, the effect of both CMWs becomes evident as L-  
518 CMW and D-CMW together account for all the  $\text{Cs}_F$  present. The prescribed 32°N cutoff in L-  
519 CMW (Fig. 9b pink curve) is clearly non-physical, and between 32°N and 40°N we are missing a  
520 significant portion of the water column with the latitude- $\sigma_0$  criteria (difference between the solid

521 red and black dotted curves) as not all water masses present are accounted for in the definitions  
 522 used.



523 **Figure 9:** a) Blue solid, red solid and black dotted curves indicate the water column inventory of  $^{137}\text{Cs}$ ,  $^{134}\text{Cs}$ ,  $^{137}\text{Cs}$ - $^{134}\text{Cs}$  in each square meter along the meridional 152°W line. Crosses indicate location where half the total inventory has been accumulated integrating from south to north. For  $^{134}\text{Cs}$  this halfway point (40.05°N) almost coincides with maximum inventory (40.75°N). For  $^{137}\text{Cs}$  the halfway point (36.35°N) is offset from the maximum (40.15°N). Red asterisk indicates FDNPP latitude; b)  $^{134}\text{Cs}$  - red curve is the same as in (a), other colored curves represent the water column inventory component for each of the water masses discussed in the text. The dotted blue curve represents the sum of all water mass components. Note, due to overlap in water mass definitions the sum can be greater than the total. Likewise, because not all water is represented by these water masses the sum can be less than the total. All values are decay corrected to April 6, 2011.

524 If the formation region  $\theta$ ,  $S$ , and  $\sigma_0$  are used to identify the L-CMW contribution, the cutoff is still  
525 at  $32^\circ\text{N}$ , but using  $\sigma_0$  alone, the sum of the D- and L-CMW contributions is one and a half times  
526 the total. Therefore, for the purpose of this inventory calculation we define the missing portion as  
527 modified CMW, which is either spicier (i.e. warmer and saltier) than newly formed D-CMW  
528 (expanding the purple Fig. 6 rectangle up and to the right) and/or less spicy (i.e. cooler and fresher)  
529 than newly formed L-CMW (expanding the orange Fig. 6 rectangle down and to the left). With  
530 this modified CMW definition, of the  $^{134}\text{Cs}$  signal at  $152^\circ\text{W}$ : 55% is associated with D-CMW, 5%  
531 is L-CMW defined to exist south of  $32^\circ\text{N}$ , 18% is modified CMW found between  $32^\circ$  and  $40^\circ\text{N}$   
532 and another 18% is TRMW most of which is carried by waters to the north of  $40^\circ\text{N}$ . STMW and  
533 GASURF contribute 3% and 7%, respectively and as of 2015 at  $152^\circ\text{W}$  less 1% of the  $^{134}\text{Cs}$  had  
534 made it into NPTW, SSURF and GAIW.

535 To compare to previous estimates, one needs an estimate of the total North Pacific inventory. We  
536 used the spring 2015 longitude limit of the  $\text{Cs}_\text{F}$  signal suggested by the Rossi et al. (2013) ensemble  
537 of simulations (see Section 3.5) to obtain a maximum western extent of  $180^\circ$ . To the east, we used  
538 the pattern of surface  $^{137}\text{Cs}$  produced by Smith et al. (2017, their figure 4, June-August panel)  
539 based P16N data combined with observations from the summer 2015 Line-P and CCGS S. W.  
540 Laurier cruises. Along with a vertical distribution based on the  $152^\circ\text{W}$  observations and an  
541 assumed average  $\text{Cs}_\text{WT}$  of  $1.5 \text{ Bq m}^{-3}$  this produces a total North Pacific inventory (date corrected  
542 to April 6, 2011) of 13.3 PBq (7.1 PBq to the west of  $152^\circ\text{W}$  and 6.2 PBq to the east).

543 There are numerous uncertainties in this calculation. If the reach of the signal to the west were  
544 10% more/less (to  $176^\circ\text{E}/176^\circ\text{W}$  instead  $180^\circ$ ) the total inventory estimate would  
545 increase/decrease by  $\sim 1$  PBq. If the magnitude of the signal to the west were 10% more/less, the  
546 western component would be  $\sim 0.7$  PBq larger/smaller. Distance matters in the broad Pacific. If the  
547 signal core to the west lies closer to  $40^\circ\text{N}$  than  $45^\circ\text{N}$ , as does the core of the eastward flow, the  
548 inventory estimate could be  $\sim 0.6$  PBq larger. A 10% larger core in the unobserved region to the  
549 southeast of  $47^\circ\text{N}$ ,  $152^\circ\text{W}$ , could further increase the estimate by  $\sim 0.5$  PBq. Therefore, a  
550 conservative range for the total  $^{134}\text{Cs}$  inventory would be 11-16 PBq. Therefore, a conservative  
551 range for the total  $^{134}\text{Cs}$  inventory would be 11-16 PBq. This range is consistent with the previous  
552 estimates discussed, e.g. the DOD + AD estimates of 15-16 PBq (Inomata et al., 2016; Tsubono et  
553 al., 2016). How much AD and DOD individually contribute to this estimate depends on how much  
554 of each signal reached the  $152^\circ\text{W}$  line as sampled here.

555 In conclusion, based on the 152°W observations, the North Pacific Cs<sub>F</sub> inventory is dominated by  
556 D-CMW and TRMW which together account for ~70% of the total. To rigorously combine the  
557 2015 meridional dataset with observations taken at different times, geographic locations and  
558 depths to compute a total inventory is nontrivial. The physical processes involved (3-dimensional  
559 transport and dispersion) are associated with strong variability at monthly, seasonal and annual  
560 time-scales making disentangling and/or correcting multiple datasets to construct an “aggregated  
561 dataset” is a complex task. That said, a related project is presently underway to combine the many  
562 ocean Cs observations now available (MARIS, 2019) to investigate the inventory distribution  
563 throughout the full basin.

### 564 **3.3 Background <sup>137</sup>Cs**

565 By focusing on the <sup>134</sup>Cs results, we have thus far avoided making a distinction between the  
566 weapons testing <sup>137</sup>Cs (<sup>137</sup>Cs<sub>WT</sub>) background and the more recent FDNPP contamination. Here, we  
567 turn our attention to <sup>137</sup>Cs<sub>WT</sub>. Note that in the following discussion, if a specific reference year is  
568 not provided (e.g. “in year value was”), values are decay corrected to April 2011.

569 In 1980, Bowen et al. published estimates of <sup>137</sup>Cs<sub>WT</sub> based on a zonal GEOSECS section between  
570 30-35°N and 140°E-120°W (i.e. crossing 152°W and henceforth referred to as GZ for GEOSECS  
571 Zonal) and a meridional section at 120-128°W, 15S°-35°N (henceforth GM), east of our section  
572 but covering some of the same latitudes (Fig. S7). On GZ at 152°W, <sup>137</sup>Cs observations suggested  
573 near surface values in 1973 of ~8.5 Bq m<sup>-3</sup>, and a subsurface maximum at 50-150 m of ~10 Bq m<sup>-3</sup>  
574 that decreased to 5 Bq m<sup>-3</sup> by 500 m and to less than 0.3 Bq m<sup>-3</sup> by ~600 m. On GM there was a  
575 fairly linear decrease with latitude at the surface from the 8.5 Bq m<sup>-3</sup> at 30-35°N to somewhere in  
576 the range of 1.7-3.4 Bq m<sup>-3</sup> at the equator. The vertical gradient was steeper further south (~5 Bq  
577 m<sup>-3</sup> at 200 m and less than 0.3 Bq m<sup>-3</sup> at 300-400 m between 0°-15°N).

578 Ignoring mixing and advection for now, by 2011 the surface values on GZ at 152°W would have  
579 decayed to 3.5 Bq m<sup>-3</sup> and the subsurface maximum to 4.3 Bq m<sup>-3</sup> (Fig. 10a, green dashed curve).  
580 Consistent with the P16N observations (Fig. 3b), the decay corrected Bowen et al. (1980) vertical  
581 gradient implies 2011 values of less than 0.1 Bq m<sup>-3</sup> at ~600 m. Livingston and Povinec (2000)  
582 reported a northeast Pacific surface <sup>137</sup>Cs value of 3 Bq m<sup>-3</sup> in 2000, which decay corrected would  
583 be 2.3 Bq m<sup>-3</sup> in 2011, or about a two-thirds of the decay corrected Bowen (1980) value.  
584 Subtracting this fractional difference between the two surface estimates from the Bowen curve

585 (Fig. 10a, green dashed curve) as a multiplicative offset gives a profile estimate for 2000 (Fig. 10a,  
 586 blue dashed curve) that assumes the shape of the profile did not change over time.

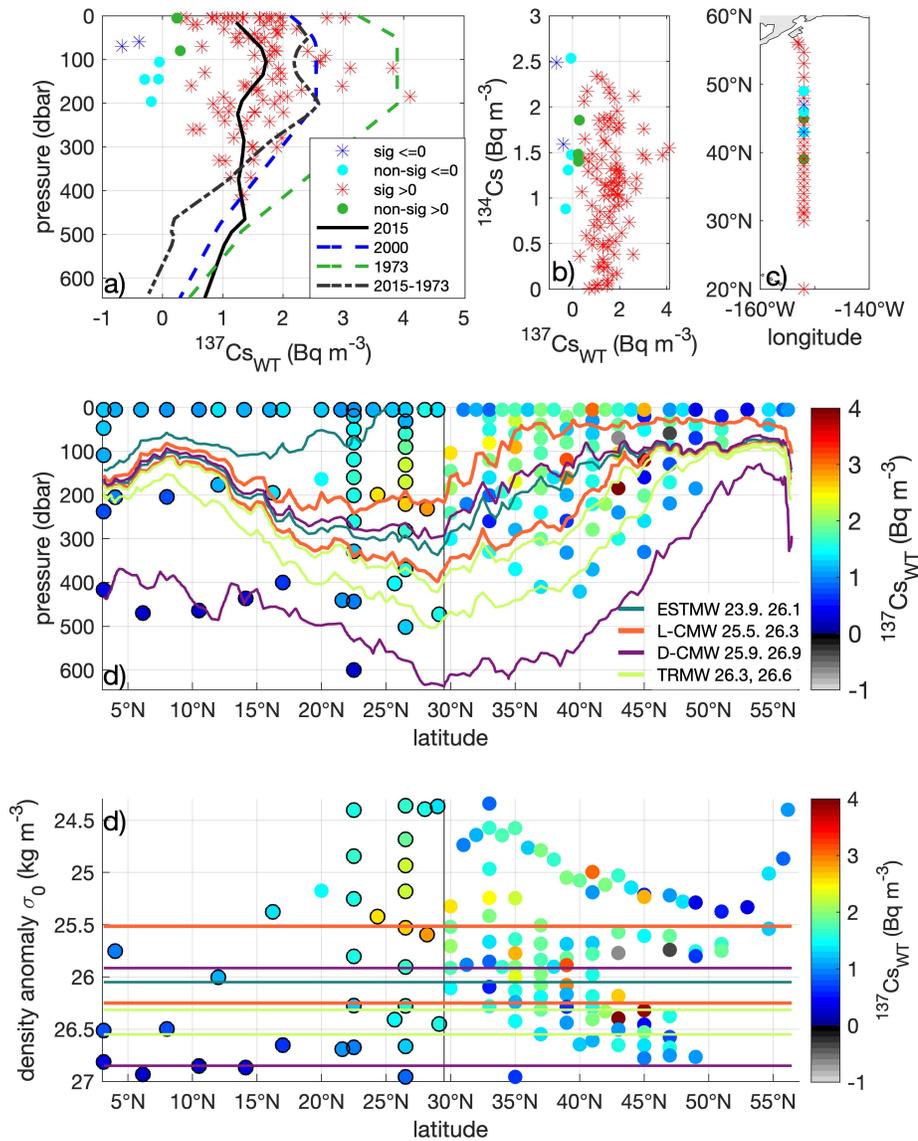


**Figure 10:** Estimates of  $152^\circ\text{W}$   $^{137}\text{Cs}$  background calculated as  $^{137}\text{Cs}_{\text{WT}} = \text{observed } ^{137}\text{Cs} \text{ minus predicted } ^{137}\text{Cs}$  (calculated from  $^{134}\text{Cs}$  observations and a decay corrected  $^{137}\text{Cs}/^{134}\text{Cs}$  ratio). a) Asterisks (circles) are values that are (not) significantly different from zero, where significant implies a 95% confidence level. Red/green (blue/cyan) symbols are greater (less) than 0. Black solid line is the weighted mean of the red asterisks. Historical estimates shown as green and blue dashed curves are explained in the text. Grey dot-dash curve is the green minus the black curves; b) Comparison of  $^{134}\text{Cs}$  to  $^{137}\text{Cs}_{\text{WT}}$  magnitude, same symbols as in (a); c) geographical location of the symbols in (a); d) latitude-pressure section of significant  $^{137}\text{Cs}_{\text{WT}}$  (i.e. red asterisks in (a)) plus to the south  $30^\circ\text{N}$  (see separating black line), observed  $^{137}\text{Cs}$  (circled in black) at locations where no  $^{134}\text{Cs}$  was detected  $^{137}\text{Cs}$ . Color contours represent water mass boundaries as in Fig. 3; e) Same as (d) in potential density anomaly-latitude space. (Units:  $\text{Bq m}^{-3}$ )

587 Here we have the opportunity to estimate the shape of the background field from the 2015  
588 observations. By decay correcting 2011 FDNPP  $^{134}\text{Cs}/^{137}\text{Cs}$  ratio (1.0, Buesseler et al., 2011) to  
589 spring 2015 and applying it to our  $^{134}\text{Cs}$  observations a predicted FDNPP-only  $^{137}\text{Cs}$  estimate can  
590 be obtained. The background  $^{137}\text{Cs}_{\text{SWT}}$  estimate is the difference between the observed and  
591 predicted  $^{137}\text{Cs}$  (Fig. 10a, colored symbols and black solid curve). We estimate the mean (cross-  
592 section area-averaged) 2011 northeast Pacific  $^{137}\text{Cs}_{\text{SWT}}$  to be  $1.2\pm 0.1 \text{ Bq m}^{-3}$  ( $1.3\pm 0.1 \text{ Bq m}^{-3}$  along  
593  $152^\circ\text{W}$ ,  $1.1\pm 0.1 \text{ Bq m}^{-3}$  across the gyre, and  $0.34\pm 0.1 \text{ Bq m}^{-3}$  in the surface waters along the short  
594 underway section off the coast of Seattle).

595 Comparing the patterns  $^{137}\text{Cs}_{\text{SWT}}$  (Fig. 10) suggest first that: a) the subsurface maximum vertical  
596 gradient reported by Bowen et al. (1980) still exists and in 2015 was on average  $2 \text{ Bq m}^{-3}$  at  $\sim 100$   
597 m; b) the surface latitudinal gradient they suggested may also still exist beginning at  $\sim 45^\circ\text{N}$ ; c)  
598 while south of  $35^\circ\text{N}$  the surface values are generally less than  $2 \text{ Bq m}^{-3}$ , the decay corrected  
599 Livingston and Povinec (2000) value and maximum surface values are slightly higher than this  
600 estimate; and d) while the magnitude of  $^{137}\text{Cs}_{\text{SWT}}$  is not dependent on the magnitude of the measured  
601  $^{134}\text{Cs}$  signal (Fig. 10b), the spread in  $^{137}\text{Cs}_{\text{SWT}}$  decreases with decreasing  $^{134}\text{Cs}$ , i.e. increasing depth.  
602 This last, speaks both to the latitudinal limits on the  $^{134}\text{Cs}$  signal at depth and to the relationship  
603 between the 4- and 40-year mixing timescales.

604 The difference between the mean profiles suggested by data from the 1970's, the 1990's and 2015  
605 is a result not only of the uncertainties in the estimates themselves but also mixing and stirring  
606 over time. Over the last 43 years the rate of non-decay related change in  $^{137}\text{Cs}_{\text{SWT}}$  (Fig. 10a, gray  
607 dot-dash curve = green curve minus black curve, henceforth  $\Delta^{137}\text{Cs}_{\text{SWT}}$ ) has developed a shape,  
608 which like the pattern of  $C_{\text{SF}}$ , is at least partially related to the mixing and advection of western  
609 basin waters. While above  $\sim 50$  m, lighter waters such as ESTMW dominate (Fig. 10d, above upper  
610 orange contour) and from 50-200 m, L-CMW contributes (below upper orange contour), the  
611 difference (the bulge in the gray dot-dash curve centered at about 100 m) is not significant. If one  
612 assumes that south of  $30^\circ\text{N}$  (black line Fig. 10d,e) where  $^{134}\text{Cs}$  is not detectable, the distribution  
613 of  $^{137}\text{Cs}$  (values circled in black Fig. 10d,e) represents  $^{137}\text{Cs}_{\text{SWT}}$ , the same conclusion holds –waters  
614 just at and above L-CMW dominate even as the isopycnals descend southward.

615 Between 1973 and 2015 the mean  $\Delta^{137}\text{Cs}_{\text{SWT}}$  above 200 m has been  $0.55\pm 0.02 \text{ Bq m}^{-3} \text{ decade}^{-1}$ .  
616 From 200-450 m (the deepest at which multiple  $^{134}\text{Cs}$  observations are available) the mean

617  $\Delta^{137}\text{C}_{\text{SWT}}$  is  $0.35 \pm 0.15 \text{ Bq m}^{-3} \text{ decade}^{-1}$  and is associated with a steady decrease between the two  
618 depths of  $14 \pm 7 \text{ Bq m}^{-3} \text{ decade}^{-1} \text{ km}^{-1}$ . As this slope is solely dependent on the Bowen et al. (1980)  
619 1973 values (the 2015 observations suggest the 200-500 m  $^{137}\text{C}_{\text{SWT}}$  is well-mixed), it suggests that  
620 western basin mixing in the transition region into which  $\text{C}_{\text{SF}}$  was discharged has been  
621 deeper/denser than that seen on average over the last 40 years. The lack of significant gradient  
622 with depth in  $\Delta^{137}\text{C}_{\text{SWT}}$  above 200 m (mid-range of western basin transition region winter MLD,  
623 Fig. S7), suggests that in the mean for these waters mixing on the 40-year and 4-year time scales  
624 are more similar. This result is consistent with Aoyama et al. (2008) who found subsurface maxima  
625 in  $^{137}\text{C}_{\text{SWT}}$  at  $165^\circ\text{N}$  in STMW and L-CMW.

### 626 3.4 What $^{90}\text{Sr}$ can and cannot tell us

627 Strontium-90 (28.79-year half-life) was also measured at some of the same locations as Cs on the  
628  $152^\circ\text{W}$  line (Fig. 11, S8a-e). Like  $^{137}\text{Cs}$ , there are two sources of  $^{90}\text{Sr}$ , namely FDNPP ( $^{90}\text{Sr}_{\text{F}}$ ) and  
629 weapons testing fallout ( $^{90}\text{Sr}_{\text{WT}}$ ). The latter has a  $^{137}\text{Cs}/^{90}\text{Sr}$  ratio of  $1.46 \pm 0.16$  (Bowen et al., 1980)  
630 and an average surface ocean  $^{90}\text{Sr}$  activity of  $\sim 1 \text{ Bq m}^{-3}$  (Povinec et al., 2012). The 2011  
631 ( $^{137}\text{Cs}/^{90}\text{Sr}$ )<sub>F</sub> ratio was much higher ( $\sim 1000$ , Castrillejo et al., 2015) for AD due to the low volatility  
632 of Sr relative to Cs and  $39 \pm 1$  ratio for DOD (Casacuberta et al., 2013; Buesseler et al., 2017).  
633 Although the AD and DOD ratios are different, observed levels of  $^{137}\text{Cs}$  were not large enough to  
634 distinguish AD and DOD fractions (Fig. S8f-g).

635 The highest 2015  $152^\circ\text{W}$   $^{137}\text{Cs}$  activities are order  $10 \text{ Bq m}^{-3}$ . Assuming this  $10 \text{ Bq m}^{-3}$  of  $^{137}\text{C}_{\text{SF}}$   
636 has been added to the existing system, then it follows that with ( $^{137}\text{Cs}/^{90}\text{Sr}$ )<sub>F</sub> ratios of 1000 and 40,  
637 an additional  $0.01$  and  $0.25 \text{ Bq m}^{-3}$  of  $^{90}\text{Sr}$  from AD and DOD would be observed, respectively.  
638 Given the  $^{137}\text{Cs}$  and  $^{90}\text{Sr}$  detection limits (see Section 2.2, and note no Cs samples sent to HADES  
639 Lab Cs measured  $^{90}\text{Sr}$ ) and the  $152^\circ\text{W}$  surface background levels of  $1\text{-}2 \text{ Bq m}^{-3}$  for  $^{137}\text{Cs}$  and  $\sim 1.3$   
640  $\text{Bq m}^{-3}$  for  $^{90}\text{Sr}$ , we can conclude that additional  $^{90}\text{Sr}_{\text{F}}$  would not be seen in the measured  $^{137}\text{Cs}/^{90}\text{Sr}$

**Figure 11:**  $^{137}\text{Cs}$  predicted from: a) observed  $^{134}\text{Cs}$  (method explained in Section 3.3) and b)  $^{90}\text{Sr}$  (method explained in Section 3.4). Solid triangles indicate predicted  $^{137}\text{C}_{\text{SWT}}$  estimates and open triangles indicate observed  $^{137}\text{C}_{\text{SF}}$ . Colors in (b) represent predicted values at different latitudes along the  $152^\circ\text{W}$  line. Note, here values are decay corrected to the day of collection. These profiles are shown individually in Fig. S8.

641 ratio. Consistent with this conclusion, only one sample had  $^{90}\text{Sr}$  elevated over background by more  
 642 than the associated measurement error (Fig S8f).

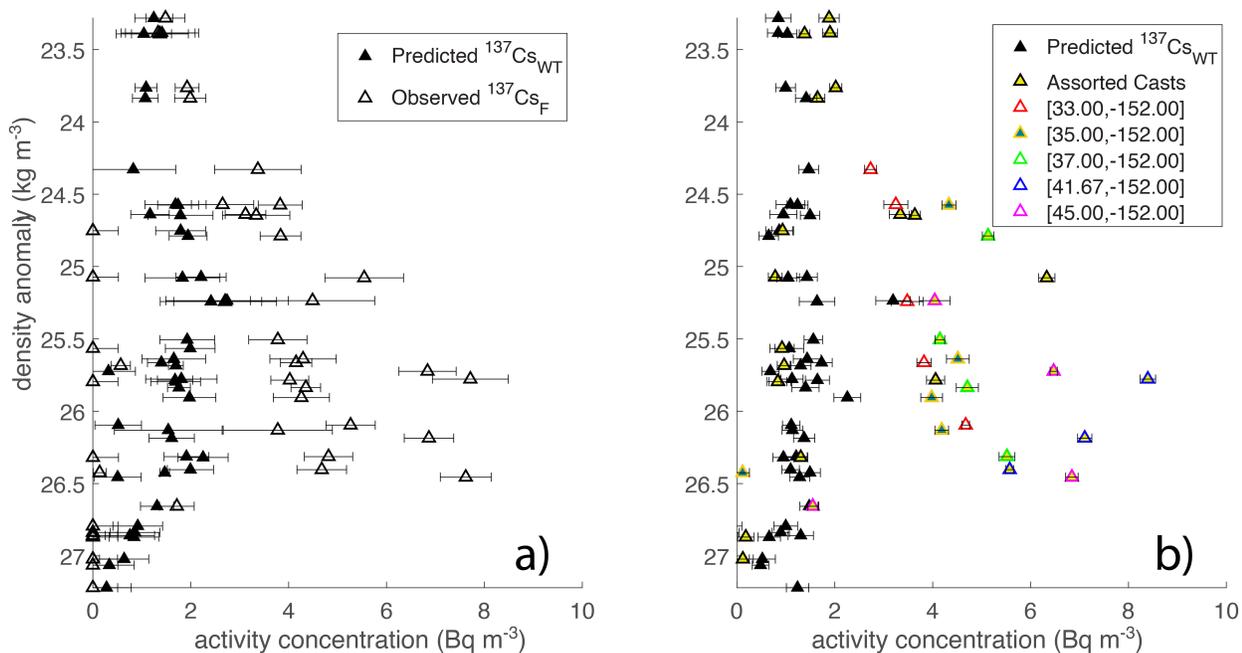


**Figure 11:**  $^{137}\text{Cs}$  predicted from: a) observed  $^{134}\text{Cs}$  (method explained in Section 3.3) and b)  $^{90}\text{Sr}$  (method explained in Section 3.4). Solid triangles indicate predicted  $^{137}\text{Cs}_{\text{SWT}}$  estimates and open triangles indicate observed  $^{137}\text{Cs}_{\text{SF}}$ . Colors in (b) represent predicted values at different latitudes along the  $152^\circ\text{W}$  line. Note, here values are decay corrected to the day of collection. These profiles are shown individually in Fig. S8.

643 If instead we assume that all measured  $^{90}\text{Sr}$  came from weapons testing, we can take advantage of  
 644 the constant  $^{137}\text{Cs}/^{90}\text{Sr}$  ratio (Fig. S8g) in that source to calculate the  $^{137}\text{Cs}_{\text{SWT}}$  and derive the  $^{137}\text{Cs}_{\text{SF}}$   
 645 component by differencing the observed  $^{137}\text{Cs}$  and estimated  $^{137}\text{Cs}_{\text{SWT}}$ . This technique is similar to  
 646 that used in Section 3.3. In fact, the  $^{90}\text{Sr}$  method has a smaller associated error and can therefore  
 647 be more useful than the  $^{137}\text{Cs}/^{134}\text{Cs}$  method deeper in the water column where radionuclide  
 648 activities are low (Fig. 11a). The  $^{90}\text{Sr}$  technique suggests similar latitudinal and density gradients  
 649 in  $^{137}\text{Cs}_{\text{SWT}}$  (Fig. 11b). In the near future, when  $^{134}\text{Cs}$  has decayed beyond measuring capabilities,  
 650  $^{90}\text{Sr}$  may be the only way to satisfactorily separate  $^{137}\text{Cs}_{\text{SWT}}$  from  $^{137}\text{Cs}_{\text{SF}}$ .

### 651 3.5 Comparison to Model Predictions

652 Based on observed density surfaces and the modeling work of Behrens et al. (2012), it was  
 653 hypothesized that deep winter mixing in the western basin and subsequent eastward advection  
 654 along isopycnal surfaces within the ocean interior would produce subsurface  $\text{Cs}_{\text{SF}}$  maxima in our

655 eastern basin observations. The depth of these maxima would depend on the ventilation intensity,  
656 i.e. the depths of winter mixed layers that occurred following the discharge. A more complete  
657 scenario would be that the predominant surface advection associated with intense mixing through  
658 a rich eddy field would be the main dynamics responsible for the first (2012-2016) invasion of  
659 surface intensified  $C_{SF}$  maxima in the eastern basin. Later (2014-2021), Cs-enriched MWs formed  
660 in the western basin during the previous winters would reach the subsurface Northeast Pacific  
661 through complex 3-dimensional pathways (Rossi et al. 2013, 2014; henceforth RET1314). The  
662 RET1314 simulations suggested that tracer concentrations would be primarily determined by the  
663 mixed layer concentrations at the time and location of MW formation, while the presence or  
664 absence of observed tracer along the sampled section would be mainly determined by the small-  
665 scale variability of interior pathways. In the Northeast Pacific, the model predicted surface  $^{137}C_{SF}$   
666 maxima of the order of  $10 \text{ Bq m}^{-3}$  to the north of  $40^\circ\text{N}$  throughout 2012-2016 period, while  
667 subsurface maxima of order of  $1 \text{ Bq m}^{-3}$  were suggested south of  $40^\circ\text{N}$  over 2014-2021 period  
668 (RET1314).

669 The RET1314 particle trajectory simulations based on the Ocean model For the Earth Simulator  
670 (OFES) eddy-resolving velocity fields, the most realistic in the region, provides an excellent  
671 qualitative of comparison between the  $152^\circ\text{W}$  observations and a model prediction (Fig. 12). Note,  
672 although we compare to model results extending to 2015, the model was not rerun for our  
673 comparison. The RET1314 model tracer is FDNPP DOD  $^{137}C_{SF}$ . The simulations used a 22 PBq  
674 point source (larger than our DOD+AD inventory estimate, Section 3.2) within 30 km of the  
675 FDNPP, assumed no background  $C_{SWT}$  and neglected AD. Despite these acknowledged  
676 limitations, there are many qualitative similarities between the observed and simulated  $152^\circ\text{W}$   $C_{SF}$   
677 signals: the latitudinal distributions as of May 2015 (Fig. 12a) are centered in generally similar  
678 location ( $\sim 25\text{-}50^\circ\text{N}$ , Fig. 12b,c); they extend to a similar depth ( $\sim 600 \text{ m}$ , Fig. 12b,c); the maximum  
679 activity is the same order of magnitude ( $\sim 10 \text{ Bq m}^{-3}$  compared to observed  $^{137}C_{SF} + ^{137}C_{SWT}$  of  $\sim 12$   
680  $\text{Bq m}^{-3}$ ); and maximum signal lies subsurface in the upper water column but includes a surface  
681 signature. That said, on closer inspection a number of both qualitative and quantitative differences  
682 become apparent.

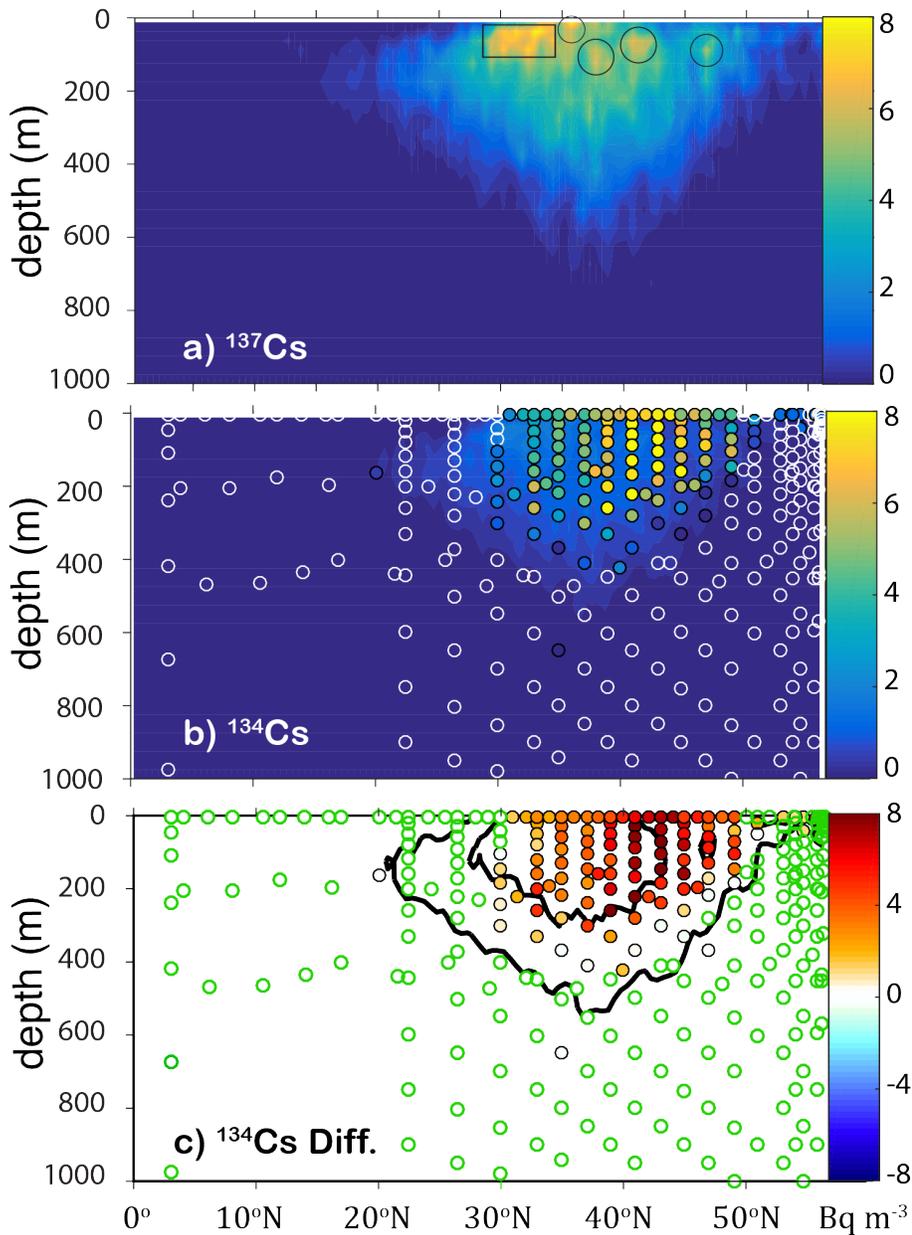


**Figure 12:** a) Model simulation estimate of May 2015 distribution of  $^{137}\text{Cs}$  along the meridional  $152^\circ\text{W}$  line, black rectangle and circles highlight higher activity cores mentioned in the text; b) the same as (a) but for  $^{134}\text{Cs}$  calculated using  $^{134}\text{Cs}/^{137}\text{Cs}$  ratio decay corrected to 2015, shaded black /empty white circles indicate observed values and non-detectable samples; c) shaded black circles indicate the observed minus model  $^{134}\text{Cs}$  differences, empty green circles indicate non-detectable samples, black contours are isolines of  $^{134}\text{Cs}$ , where the outer line ( $0.25 \text{ Bq m}^{-3}$ ) broadly represents the edge of model simulated plume and the inner line ( $1.0 \text{ Bq m}^{-3}$ ) highlights the core of the simulated plume. Note,  $-8$  to  $8 \text{ Bq m}^{-3}$  color axis highlights the positive nature of these differences.

684 While the maxima are similar, the source estimates for the model (22 PBq) and observations (11-  
685 16 PBq) are different. Scaling the model maximum by the ratio of the estimated source sizes results  
686 in a model prediction ( $\sim 5\text{-}7 \text{ Bq m}^{-3}$ ) that is half what is observed. Also, the  $152^\circ\text{W}$  distribution  
687 details are different. While the model distribution of  $^{137}\text{Cs}_{\text{SF}}$  contains pockets of higher subsurface  
688 values at about  $37^\circ\text{N}$ ,  $41^\circ\text{N}$ , and possibly,  $47^\circ\text{N}$  at 50-125 m (Fig. 12a, northern circles), the major  
689 core lies to the south at  $30\text{-}35^\circ\text{N}$ , 0-100 m (Fig. 12a rectangle) and the maximum lies very close  
690 to the surface (upper right corner of rectangle and southernmost circle). The observed maximum  
691 core lies at  $41\text{-}44^\circ\text{N}$  0-200 m with a maximum at 100 m (Figs. 3b, 12b). Note, however, that due  
692 to the differences in magnitude there are few locations where simulated values are greater than  
693 observed values (Fig. 12c).

694 The above  $^{137}\text{Cs}_{\text{SF}}$  comparison provides insights into the “bigger picture” and continuity with the  
695 earlier literature – RET1314 and others who discuss these works, but comparing observed and  
696 modeled  $^{134}\text{Cs}_{\text{SF}}$  is more rigorous because there is no measurable  $^{134}\text{Cs}_{\text{WT}}$ . Applying the same  
697  $^{134}\text{Cs}/^{137}\text{Cs}$  ratio used in Section 3.3 to the RET1314 estimates highlights the differences between  
698 the modeled particle trajectory results and the observations (Fig 12b). The observed  $^{134}\text{Cs}_{\text{SF}}$   
699 (maximum of  $\sim 10 \text{ Bq m}^{-3}$ ) is significantly greater than that modeled ( $\sim 3.5 \text{ Bq m}^{-3}$ , 1.8 - 2.5 scaling  
700 by estimated source size ratio) resulting in observed minus modeled differences that are positive  
701 everywhere in the region of the cores (Fig. 12c).

702 The differences in the center of the stronger southern modeled core ( $30^\circ\text{-}35^\circ\text{N}$ ) are actually  
703 somewhat less than those found to the north because the mid-range observed signal has about the  
704 same magnitude as the most intense modeled values. There is not only a north/south offset in the  
705 location of the core (see the offset of the inner black contour from the darkest shaded circles in  
706 Fig. 12c), but the modeled signal is also more diffuse than the observed, particularly to the south  
707 where there is no indication of the observed  $^{134}\text{Cs}$   $30^\circ\text{N}$  cutoff (see southward extension of the  
708 outer black contour (Fig. 12c). To the north, we note that the Alaska Current signal is missing from  
709 the model (Fig. 12b, see shaded circles north of  $50^\circ\text{N}$ ). The specific dynamics that would go into  
710 explaining the mismatches are not straightforward because as emphasized by Rossi et al. (2013),  
711 the processes that produce the distribution depend both on remote effects (e.g. three-dimensional  
712 MW pathways and tracer concentration, primarily acquired at the time and location of MW  
713 formation) and on local effects (e.g. upwelling strength, mean depth of upwelling sources, local  
714 lateral advection and mixing (see also Smith et al. (2017)).

715 **Modeled vs. actual velocity fields:** The latitudinal locations of the Kuroshio, the KE and KBF and  
716 the diffusive nature of the model are all likely reasons for the differences between the observed  
717 and modeled distributions. The modeled results indeed consist of an ensemble of simulations  
718 (averaging out the pathways of multiple years of currents (1980-2008), i.e. multiple latitudinal  
719 locations of the core axes) and multiple years of western basin water mass formation that do not  
720 include those from the actual 2011-2015 period. It is the “ensemble approach” that produces an  
721 overall more diffuse pattern and contributes to the pronounced southward extension of the modeled  
722 cores along 152°W as it “aggregates” different cores together, allowing for more opportunities for  
723 crossing the subtropical and subpolar gyre boundaries before arrival in the eastern basin.

724 **Modeled vs. actual water mass formation:** A possible contributor to the more southerly model  
725  $C_{SF}$  core is that between 1980 and 2008 more modeled L-CMW formed in the transition region  
726 (Fig. 1) than between 2011 and 2012 (Kumamoto et al., 2014; Kaeriyama et al., 2016; Cedarholm  
727 et al., 2019), which would result in a more southerly eastward flow of  $C_{SF}$  (Oka and Qiu, 2012).  
728 This highlights the non-negligible role of the prominent inter-annual variability of MW formation  
729 and its effect on our understanding of the long-term fate of oceanic tracers and properties.

730 **Modeled vs. actual tracer source:** Another difference between modeled and observed  $C_S$   
731 distributions is that the model did not include an AD source as it was poorly understood at the time  
732 the model runs were performed. The fact that the southern core in the model is overestimated  
733 suggests that modeled L-CMW has carried a substantial portion of the DOD signal across the  
734 basin. The region of maximum AD was to the northwest of the FDNPP (e.g. Stohl et al., 2012),  
735 that is, in the region of denser D-CMW/TRMW formation. Therefore, by neglecting such surface  
736 inputs, the model underestimates the northern core as compared to the strong D-CMW signal seen  
737 in the observations. Following this train of thought, it suggests that AD may be the dominant  
738 source of the 152°W signal.

739 RET1314 projected that the portion of  $^{137}C_{SF}$  that had been subducted into the interior ocean would  
740 return to the surface via coastal upwelling along the west coast of North America, some years after  
741 the initial surface report in 2012-2013 that was solely due to horizontal currents. They suggested  
742 that this process would take about 6-9 years after DOD, that is 2017-2021 (later than 2015). If, as  
743 discussed above, the bulk of modeled signature was advected in L-CMW on the inside edge of the  
744 subtropical gyre, rather than D-CMW/TRMW on the outside edge, its arrival in the north would

745 have be slowed. It is also interesting to consider the lone  $^{134}\text{Cs}$  observation obtained at  $20^\circ\text{N}$ . The  
746 model, like the observations, finds the tracer signal to be subsurface at this latitude, and as the  
747 model does not include AD, its signal cannot be AD mixed down into ESTMW in 2011, but must  
748 instead have been DOD advected in lighter waters.

749 It is worth noting that other factors contributing to the differences are the patchiness of tracer  
750 distributions in the real ocean associated with the discrete and non-synoptic sampling that could  
751 bias the “observational” perspective. Indeed, if a southern core exists, it is possible that the  
752 sampling missed it due to submesoscale variability in the real ocean. From this perspective, our  
753 model-data comparison highlights how the model prediction and observations complement each  
754 other to reconstruct the “true” tracer fate.

#### 755 **4. Summary and Conclusions**

756 In 2015, nearly 400 individual samples for measurement of radionuclides ( $^{134}\text{Cs}$ ,  $^{137}\text{Cs}$ ,  $^{90}\text{Sr}$ ) were  
757 collected along  $152^\circ\text{W}$ , across the Alaska Gyre and on a 200 nautical mile transect in the EEZ off  
758 Seattle. The samples presented maximum magnitudes, decay corrected to April 2011, of order of  
759  $10\text{ Bq m}^{-3}$  ( $^{134}\text{Cs}$ ),  $12\text{ Bq m}^{-3}$  ( $^{137}\text{Cs}$ ) and  $2.5\text{ Bq m}^{-3}$  ( $^{90}\text{Sr}$ ). These radionuclide tracers carry a  
760 signature of MW formed in the northwest 3-4 years earlier after they had traversed some 7500 km  
761 beneath the surface to arrive at  $152^\circ\text{W}$ . Here, these waters penetrate to about 300 m at  $30^\circ\text{N}$ , 400  
762 m at  $40^\circ\text{N}$ , and shoal with the density surfaces that rise toward the North American coast. Covering  
763 the distance between the FDNPP and  $35^\circ\text{N}$ ,  $152^\circ\text{W}$  (location of deepest  $^{134}\text{Cs}$ ) in 4 years suggests  
764 a cross-basin advection speed that averages about  $4.8\text{ cm s}^{-1}$ . This is faster than the mean western  
765 basin  $3\text{ cm s}^{-1}$  reported by Oka et al. (2011), but similar to the estimates reported by Kumamoto et  
766 al. (2019) for  $^{137}\text{Cs}$  export from the western basin in 2011. Interestingly, it is also similar to the  $4.6$   
767  $\text{cm s}^{-1}$  reported by Taguchi et al. (2014) as the average 0-400 m eastward propagation speed of  
768 ocean heat content anomalies crossing the basin between  $40^\circ\text{N}$  and  $48^\circ\text{N}$  (see their figure 1). This  
769 comparison brings the discussion full circle – back to one motivation for this study mentioned in  
770 the introduction (Section 1.1): information about MW circulation gleaned from  $\text{C}_{\text{SF}}$  could be useful  
771 to our understanding of MW impacts on other surface-related variables such as oxygen utilization,  
772 carbon uptake and storage rates, as well as sea-surface temperature variability.

773 The observations suggest that more than half the  $\text{C}_{\text{SF}}$  was brought to  $152^\circ\text{W}$  in D-CMW with  
774 significant, but smaller, contributions supplied by TRMW, L-CMW, and a modified version of

775 either or both varieties of CMW. There was a clear cutoff in the  $C_{SF}$  signature at  $30^{\circ}N$ , the  
776 estimated northern limit of subtropical and tropical waters, indicating that CMW's stayed within  
777 the North Pacific Current over this time frame and did not diffuse southward west of this longitude.  
778 This result is consistent with analysis of Argo float profiles, but inconsistent with the model-based  
779 particle trajectory experiments of Rossi et al. (2013, 2014). The core of the strongest  $C_{SF}$  signal  
780 ( $39^{\circ}$ - $45^{\circ}N$ ) extended from just below the surface to  $\sim 260$  m.  $C_{SF}$  observations also indicated  
781 transport of a weak surface signal around the Alaska Gyre in the boundary current and an upwelling  
782 of  $C_{SF}$  near the Seattle coast, which is consistent with Line-P findings (e.g. Smith et al., 2015,  
783 2017). The  $152^{\circ}W$  observations suggest a basin-wide 2011 Cs inventory of 11-16 PBq.

784 The  $^{137}Cs$  observations support the results found using FDNPP fingerprint of  $^{134}Cs$  and also  
785 provide some information about the weapons testing background. Using all P16N  $^{134}Cs$   
786 measurements we find a mean 2011 Northeast Pacific  $^{137}C_{SWT}$  activity of  $1.2 \pm 0.1$  Bq  $m^{-3}$  (at  $152^{\circ}W$   
787 the mean  $^{137}C_{SWT}$  is  $1.3 \pm 0.1$  Bq  $m^{-3}$ ). Over the last half century, this weapons signal has penetrated  
788 down to 900-1000 m in the Alaska Gyre (the deepest detection between  $37^{\circ}N$  and  $50^{\circ}N$ ) and to  
789  $\sim 400$  m throughout the subtropical gyre and into the tropics. Earlier studies reported a latitudinal  
790 dependence for  $^{137}C_{SWT}$  in the Northeast Pacific and the 2015 Cs and Sr both suggest that this  
791 dependence, although weaker than a few decades ago, appears to have been retained.

792 The analysis of  $152^{\circ}W$  2015 Cs suggests that it was the denser variety of mode waters (D-  
793 CMW/TRMW) that brought most of the signal eastward. Analyses of ARGO floats show that this  
794 is because there was formation of denser than usual waters in the transition region in the 2011-  
795 2012 timeframe. As observed by others (e.g. Inomata et al., 2018; Aoyama et al., 2016a), these  
796 waters were advected into the North Pacific Current. The comparison to the DOD based  
797 simulations of RET1314 suggests that this D-CMW/TRMW signal may also be attributable to  
798 western basin AD, rather than DOD. Although some evidence of L-CMW (commonly formed in  
799 the transition region) is seen at  $152^{\circ}W$ , with the clear cutoff in the  $C_{SF}$  at  $30^{\circ}N$  (the boundary with  
800 both E-STMW and subtropical gyre waters) it is likely that the bulk of  $C_{SF}$  in L-CMW was  
801 subducted and advected eastward on southern side of the KE, and drawn into the western basin  
802 recirculation. Unlike  $C_{SF}$  (4-year timescale), weapons testing background (50-year timescale) does  
803 appear to be associated with L-CMW. This result is consistent with analysis of observations at  
804  $165^{\circ}E$  (Aoyama et al. 2008).

805 The release of  $\text{Cs}_{\text{F}}$  has afforded the opportunity to employ a powerful, soluble, readily detectable  
806 tracer discharged into the ocean at a known time and location to better understand North Pacific  
807 dynamics. Moving beyond the question of the extent and speed with which FDNPP radioactivity  
808 has spread, we have begun to examine what this unique tracer can tell us about the underlying  
809 physical processes and evolution of the 2011 vintage of MWs. Future efforts will look to combine  
810 these 2015 observations with other data collected across the basin as well as model output and  
811 non-radionuclide water property observations. Together, these data will allow investigation into  
812 the role of North Pacific MW in transporting, mixing and storing the characteristics they gain from  
813 the atmosphere at the time of formation and will improve our understanding of the MW role in the  
814 cycles associated with ocean heat content, biological production, nutrient cycling as well as  $\text{CO}_2$   
815 uptake and ocean acidification.

816 **Acknowledgements:** We thank the science parties and crew of the National Oceanic and  
817 Atmospheric Administration (NOAA) ship Ronald Brown, which occupied the 2015 repeat of the  
818 P16N line, for their assistance in obtaining water samples for radiocesium measurement. In  
819 particular, we thank Samantha Siedlecki, leg 1 co-chief scientist, for her assistance in obtaining  
820 the 27 samples to the south of Hawaii, Jessica Cross, leg 1 chief scientist, for her diplomatic  
821 assistance with logistics in Tahiti, Jessica Drysdale not only for measuring the radionuclides in the  
822 2015 samples, decay correcting and collating the results, but also for her tremendous assistance in  
823 organizing shipment of samples to Europe and Brendan Carter for discussion on inventories. All  
824 WHOI-based co-authors acknowledge salary and project support from the National Science  
825 Foundation (NSF) grant OCE#-1356630 and OCE#-1923387. Pike's participation in the 2015  
826 P16N cruise was supported through this same grant and Macdonald's participation was supported  
827 by NSF grant OCE#-1437015. We acknowledge additional salary support for Buesseler from the  
828 Deerbrook Charitable Trust and Kenyon from an NSF Graduate Research Fellowship under grant  
829 #1122374. Rossi acknowledges Australia's University of New South Wales (UNSW) as some  
830 modelling aspects of this research were generated using the Linux computational cluster Katana  
831 supported by the Faculty of Science at UNSW. We thank the personnel at the HADES  
832 Underground Laboratory (HADES, 2020) for their efforts in providing us with low-level isotope  
833 measurements. The HADES work was supported by the European Commission within  
834 HORIZON2020 via the EURATOM project EUFRAT for transnational access. We wish to  
835 acknowledge the more than 350 individuals and groups who contributed to the Our Radioactive

836 Ocean crowd funding campaign (ORO, 2013) and the collaborative efforts of personnel from both  
837 NOAA and NSF for making it possible for us to obtain the two extra days of ship time needed to  
838 perform the Cs-only casts on P16N. No analysis of these data was performed while onboard the  
839 NOAA vessel. Last, but no means least, we extend our sincere thanks to our reviewers and the  
840 journal's editor-in-chief, all of whom gave us the gift of careful reading, thoughtful critique and  
841 astute insights.

842 **Data Sources and Availability:** The P16N dataset, including the Cs measurements, was collected  
843 through the U.S. GO-SHIP program (<https://usgoship.ucsd.edu/>) and made freely available  
844 through CCHDO (2019). The Cs measurements have also been contributed to MARIS (2019)  
845 through which they are also freely available. The Argo float profiles were collected and are made  
846 freely available by the International Argo Program and the national programs that contribute to it.  
847 (<http://www.argo.ucsd.edu>, <http://argo.jcommops.org>). The Argo Program is part of the Global  
848 Ocean Observing System.

849 **Contributions:** A. Macdonald organized the collection of the P16N Cs data set, performed the  
850 physical analysis of the Cs data, wrote the manuscript and created all figures except those  
851 mentioned below. S. Yoshida, I. Rypina contributed in the physical analysis of the Cs  
852 observations. S. Pike collected and shipped the P16N samples, measured many of the samples,  
853 produced the original Cs data set and wrote the section on the chemical analysis. K. O. Buesseler  
854 led the chemical analysis and contributed to the chemistry described herein. S. Jayne contributed  
855 expertise on the mode water formation region and Northwest Pacific circulation. V. Rossi provided  
856 the model-based particle tracking results and figures, and contributed to the text on the same. J.  
857 Kenyon provided the figures and contributed the text pertaining to <sup>90</sup>Sr. All co-authors contributed  
858 through comments, suggestions and the editing of the full manuscript.

## 859 **References**

- 860 1. Aarkrog, A. (2003). Input of anthropogenic radionuclides into the World Ocean. *Deep-Sea*  
861 *Res. II*, **50**, 2597–2606.
- 862 2. Aoyama, M., and D. Hirose (2008). Radiometric determination of anthropogenic  
863 radionuclides in seawater. In *Analysis of environmental radionuclides*, Povinec, P. P. (Ed.).  
864 **11**, 137–162.
- 865 3. Aoyama, M., D. Hirose, K. Nemoto, Y. Takasuki, and D. Tsumune (2008). Water masses  
866 labeled with global fallout <sup>137</sup>Cs formed by subduction in the North Pacific. *Geophys. Res.*  
867 *Letts*, **35**, L01604, doi:10.1029/2007GL031964.

- 868 4. Aoyama, M., M. Fukasawa, K. Hirose, Y. Hamajima, T. Kawano, P. P. Povinec, J. A.  
869 Sanchez-Cabeza (2011). Cross equator transport of  $^{137}\text{Cs}$  from North Pacific Ocean to South  
870 Pacific Ocean (BEAGLE2003 cruises). *Prog. Oceanogr.*, **89**, 7–16.
- 871 5. Aoyama, M., D. Tsumune, and Y. Hamajima (2012). Distribution of  $^{137}\text{Cs}$  and  $^{134}\text{Cs}$  in the  
872 North Pacific Ocean: Impacts of the TEPCO Fukushima-Daiichi NPP accident. *J. Radioanal.*  
873 *Nucl. Chem.*, doi:10.1007/s10967-012-2033-2.
- 874 6. Aoyama, M., M. Uematsu, D. Tsumune, and Y. Hamajima (2013). Surface pathway of  
875 radioactive plume of TEPCO Fukushima NPP1 released  $^{134}\text{Cs}$  and  $^{137}\text{Cs}$ . *Biogeosciences*,  
876 **10**, doi:10.5194/bg-10-3067-2013.
- 877 7. Aoyama, M. Y. Hamajima, M. Hult, M. Uematsu, E. Oka, D. Tsumune, and Y. Kumamoto  
878 (2016a).  $^{134}\text{Cs}$  and  $^{137}\text{Cs}$  in the North Pacific Ocean derived from the March 2011 TEPCO  
879 Fukushima Dai-ichi Nuclear Power Plant accident, Japan. Part one: surface pathway and  
880 vertical distributions. *J. Oceanogr.*, **72**, 53-65, doi: 10.1007/s10872-015-0335-z.
- 881 8. Aoyama, M., M. Kajino, T. Y. Tanaka, T. T. Sekiyama, D. Tsumune, T. Tsubono,  
882 Y. Hamajima, Y. Inomata, and T. Gamo (2016b).  $^{134}\text{Cs}$  and  $^{137}\text{Cs}$  in the North Pacific Ocean  
883 derived from the TEPCO Fukushima Dai-ichi Nuclear Power Plant accident, Japan in March  
884 2011: part Two – Estimation of  $^{134}\text{Cs}$  and  $^{137}\text{Cs}$  inventories in the North Pacific Ocean. *J.*  
885 *Oceanogr.* **72**, 67–76, doi:10.1007/s10872-015-0332-2.
- 886 9. Aoyama, M., Y. Inomata, D. Tsumune and Y. Tateda (2019) Fukushima radionuclides in the  
887 marine environment from coastal region of Japan to the Pacific Ocean through the end of  
888 2016. *Prog. in Nuclear Science and Technology*, **6**, 1-7, doi: 10.15669/pnst.6.1.
- 889 10. Argo (2019), Argo Information Centre, <http://www.argo.net/>
- 890 11. Behrens, E., F. U. Schwarzkopf, J. F. Lübbecke, and C. W. Böning (2012). Model  
891 simulations on the long-term dispersal of  $^{137}\text{Cs}$  released into the Pacific Ocean off  
892 Fukushima. *Environ. Res. Lett.*, **7**, doi:10.1088/1748-9326/7/3/034004.
- 893 12. Bingham, F. M., and T. Suga (2006). Distributions of mixed layer properties in North Pacific  
894 water mass formation areas: comparison of Argo floats and World Ocean Atlas 2001. *Ocean*  
895 *Sci.*, **2**, 61–70.
- 896 13. Bowen, V. T., V. E. Noshkin, H. D. Livingston, and H. L. Volchok (1980). Fallout  
897 radionuclides in the Pacific Ocean: Vertical and horizontal distributions, largely from  
898 GEOSECS stations, *Earth Planet. Sci. Lett.*, **49**, 411–434.
- 899 14. Breier, C.F., Pike, S.M., Sebesta, F., Tradd, K., Breier, J.A., Buesseler, K.O. (2016). New  
900 applications of KNiFC-PAN resin for broad scale monitoring of radiocesium following the  
901 Fukushima Dai-ichi nuclear disaster. *J. Radioanal. Nucl. Chem.*, **307**, 2193-2200.
- 902 15. Buesseler, K. O., M. Aoyama, and M. Fukasawa (2011). Impacts of the Fukushima nuclear  
903 power plants on marine radioactivity. *Environ. Sci. Technol.*, **45**, 9931–9935.
- 904 16. Buesseler, K. O., S. R. Jayne, N. S. Fisher, I. I. Rypina, H. Baumann, Z. Baumann, C. F.  
905 Breier, E. M. Douglass, J. George, A. M. Macdonald, H. Miyamoto, J. Nishikawa, S. M.  
906 Pike, and S. Yoshida (2012). Fukushima-derived radionuclides in the ocean and biota off  
907 Japan, *Proc. Nat. Acad. Sci.*, **109**, 5984–5988, doi:10.1073/pnas.1120794109.

- 908 17. Buesseler, K. O., M. Dai., M. Aoyama, C. Benitez-Nelson, S. Charmasson, K. Higley, V.  
909 Maderich, P. Masqué, P. J. Morris, D. Oughton, and J. N. Smith (2017). Fukushima-derived  
910 radionuclides in the ocean: transport, fate, impacts. *Annu. Rev. Mar. Sci.* 2017.9:173-203,  
911 doi: 10.1146/annurev-marine-010816-060733.
- 912 18. Butler, D. (2011). Radioactivity spreads in Japan, *Nature*, **471**, 555–556,  
913 doi:10.1038/471555a.
- 914 19. Casacuberta, N., P. Masqué, J. Garcia-Orellana, R. Garcia-Tenorio, and K.O. Buesseler  
915 (2013).  $^{90}\text{Sr}$  and  $^{89}\text{Sr}$  in seawater off Japan as a consequence of the Fukushima Dai-ichi  
916 nuclear accident. *Biogeosciences*, **10**, 3649-3659, doi: 10.5194/bg-10-3649-201.
- 917 20. Castrillejo M., N. Casacuberta, C. F. Breier, S. M. Pike, P. Masqué, K. O. Buesseler (2015).  
918 Reassessment of  $^{90}\text{Sr}$ ,  $^{137}\text{Cs}$ , and  $^{134}\text{Cs}$  in the coast off Japan derived from the Fukushima  
919 Dai-Ichi nuclear accident. *Environ. Sci. Technol.* **50**, 173–80.
- 920 21. CCHDO (2019). CLIVAR and Carbon Hydrographic Data Office, <https://cchdo.ucsd.edu/>.
- 921 22. Cedarholm, E. R., I. I. Rypina, A. M. Macdonald and S. Yoshida (2019). Investigating  
922 subsurface pathways of Fukushima Cs in the Northwest Pacific, *Geophys. Res. Lett.*,  
923 doi:10.1029/2019GL082500.
- 924 23. Chino, M., H. Nakayama, H. Nagai, H. Terada, G. Katata, and H. Yamazawa (2011).  
925 Preliminary estimation of release amounts of  $^{131}\text{I}$  and  $^{137}\text{Cs}$  accidentally discharged from the  
926 Fukushima Daiichi Nuclear Power Plant into the atmosphere. *J. Nucl. Sci. Tech.*, **48**, 1129–  
927 1134.
- 928 24. Conkright M. E., R. A. Locarnini, H. E. Garcia, T. D. O'Brien, T. P. Boyer, C. Stephens,  
929 and J. I. Antonov (2002). World Ocean Atlas 2001: Objective Analysis, Data Statistics and  
930 Figures CD-ROM Documentation, 17 pp., National Oceanographic Data Center, Silver  
931 Spring, MD.
- 932 25. Dong, D., P. Brandt, P. Chang, F. Schütte, X. Yang, J. Yan, and J. Zeng (2017). Mesoscale  
933 eddies in the Northwestern Pacific Ocean: Three-dimensional eddy structures and heat/salt  
934 transports. *J. Geophys. Res.*, 122, 9795–9813. <https://doi.org/10.1002/2017JC013303>
- 935 26. Garraffo, Z. D. , H-C. Kim, A. Mehra, T. Spindler, I. Rivin, and H. L., Tolman (2014).  
936 Modeling of  $^{137}\text{Cs}$  as a tracer in a regional model for the Western Pacific, after the  
937 Fukushima Daiichi Nuclear power plant accident of March 2011, *Weather Forecast.*, doi:  
938 10.1175/WAF-D-13-00101.1.
- 939 27. GODAS, (2015). National Centers for Environmental Prediction Global Ocean  
940 Data Assimilation System (GODAS) Monthly and Annual Mean Products,  
941 <https://www.cpc.ncep.noaa.gov/products/GODAS/monthly.shtml>.
- 942 28. HADES (2020). HADES Underground Laboratory,  
943 <https://science.sckcen.be/en/Facilities/HADES>
- 944 29. Hautala, S. L., D. H. Roemmich (1998). Subtropical mode water in the Northeast Pacific  
945 Basin. *J. Geophys. Res.*, **103**, 13055-13066, doi: 10.1029/98JC01015
- 946 30. Holte, J., L. Talley, J. Gilson and D. Roemmich, (2017). An Argo mixed layer climatology  
947 and data base. *Geophys. Res. Lett.*, doi:10.1002/2017GL073426.

- 948 31. Inomata, Y., M. Aoyama, and K. Hirose (2009). Analysis of 50-y record of surface  $^{137}\text{Cs}$   
949 concentrations in the global ocean using the HAM-global database, *J. Environ. Monit.*, **11** (1).  
950 116–125.
- 951 32. Inomata, Y., M., Aoyama, T. Tsubono, D. Tsumune, and K. Hirose (2016). Spatial and  
952 temporal distributions of  $^{134}\text{Cs}$  and  $^{137}\text{Cs}$  derived from the TEPCO Fukushima Daiichi  
953 nuclear power plant accident in the North Pacific Ocean by using optimal interpolation  
954 analysis. *Environ. Sci. Process. Impacts*, **18**, 126-36
- 955 33. Inomata, I., M. Aoyama, T. Tsubono, D. Tsumune, Y. Kumamoto, H. Nagai, T. Yamagata,  
956 M. Kajino, Y. T. Tanaka, T. T. Sekiyama, E. Oka and M. Yamada (2018). Estimate of  
957 Fukushima-derived radiocaesium in the North Pacific Ocean in summer 2012. *J.*  
958 *Radioanalytical and Nuclear Chemistry*, **318**, 1587–1596, doi: 10.1007/s10967-018-6249-7.
- 959 34. Kameník, J., H. Dulaiova, K. O. Buesseler, S. M. Pike, and K. Štátná (2013). Cesium-134  
960 and 137 activities in the central North Pacific Ocean after the Fukushima Dai-ichi nuclear  
961 power plant accident. *Biogeosciences Discuss*, 10, 5223-5244, doi:10.5194/bgd-10-5223-  
962 2013.
- 963 35. Kaeriyama, H., Y. Shimizu, D. Ambe, M. Masujima, Y. Shigenobu, K. Fujimoto, T. Ono, K.  
964 Nishiuchi, T. Taneda, H. Kurogi, T. Setou, H. Sugisaki, T. Ichikawa, K. Hidaka, Y. Hiroe, A.  
965 Kusada, T. Kodama, M. Kuriyama, H. Morita, K. Nakata, K. Morinaga, T. Morita, and T.  
966 Watanabe (2014). Southwest intrusion of  $^{134}\text{Cs}$  and  $^{137}\text{Cs}$  derived from the Fukushima Dai-  
967 ichi Nuclear Power Plant Accident in the western North Pacific, *Environ. Sci. Technol.*, **48**,  
968 3120–3127.
- 969 36. Kaeriyama, H., Y. Shimizu, T. Setou, Y. Kumamoto, M. Okazaki, D. Ambe, and T. Ono  
970 (2016). Intrusion of Fukushima-derived radiocaesium into subsurface water due to formation  
971 of mode waters in the North Pacific. *Sci. Rep.*, **6**, doi: 10.1038/srep22010.
- 972 37. Katsura, S., E. Oka, B. Qui, and N. Schneider (2013). Formation and subduction of North  
973 Pacific Tropical Water and their Interannual Variability. *J. Phys. Oceanogr.*, **43**, 2400-2415.
- 974 38. Katsura, S. (2018). Properties, formation, and dissipation of the North Pacific Eastern  
975 Subtropical Mode Water and its impact on interannual spiciness anomalies. *Prog. Oceanogr.*,  
976 **162**, 120-131, doi: <https://doi.org/10.1016/j.pocean.2018.02.023>
- 977 39. Kawakama, Y., S. Sugimoto, and T. Suga (2016). Inter-annual zonal shift of the formation  
978 region of the lighter variety of the North Pacific Central Mode Water. *J. Oceanogr.*, **72**, 225–  
979 234, doi: 10.1007/s10872-015-0325-1.
- 980 40. Kouketsu, S., I. Kaneko, T. Kawano, H. Uchida, T. Doi, and M. Fukasawa (2007). Changes  
981 of North Pacific Intermediate Water properties in the subtropical gyre. *Geophys. Res. Lett.*,  
982 **34**, doi:10.1029/2006GL028499.
- 983 41. Kumamoto Y, M. Aoyama, Y. Hamajima, Y. Aono, S. Kouketsu, A. Murata, and T. Kawano  
984 (2014). Southward spreading of the Fukushima-derived radiocesium across the Kuroshio  
985 Extension in the North Pacific. *Sci Rep*. doi: 10.1038/srep04276.
- 986 42. Kumamoto, Y., M. Aoyama, Y. Hamajima, S. Nishino, A. Murata, and T. Kikuchi (2016b).  
987 Meridional distribution of Fukushima-derived radiocesium in surface seawater along a trans-

- 988 Pacific line from the Arctic to Antarctic Oceans in summer 2012, *J. Radioanal. Nucl.*  
989 *Chem.*, **307**, doi:10.1007/s10967-015-4439-0.
- 990 43. Kumamoto, Y., M. Aoyama, Y. Hamajima, H. Nagai, T. Yamagata, Y. Kawai, E. Oka, A.  
991 Yamaguchi, K. Imai and A. Murata (2017). Fukushima-derived radiocesium in the  
992 western North Pacific in 2014. *J Radioanal. Nucl. Chem*, **311**, 1209–1217, doi:  
993 10.1007/s10967-016-5055-3.
- 994 44. Kumamoto, Y., M. Yamada, M. Aoyama, Y. Hamajima, H. Kaeriyamae, H. Nagai, T.  
995 Yamagata, A. Murataa, and Y. Masumoto (2019). Radiocesium in North Pacific coastal and  
996 offshore areas of Japan within several months after the Fukushima accident. *J. Environmental*  
997 *Radioactivity*, **198**, 79-88, doi: 10.1016/j.jenvrad.2018.12.015.
- 998 45. Kwon, E. Y., C. Deutsch, S.-P. Xie, S. Schmidtko, and Y.-K. Cho (2016). The North  
999 Pacific oxygen uptake rates over the past half century, *J. Climate*, **29**, 61-76, doi:  
1000 10.1175/JCLI-D-14-00157.1.
- 1001 46. Kyodo News, (2018). Seven years on, radioactive water still flows into the water, study  
1002 finds. *The Japan Times*, March 29 2018,  
1003 [https://www.japantimes.co.jp/news/2018/03/29/national/seven-years-radioactive-water-](https://www.japantimes.co.jp/news/2018/03/29/national/seven-years-radioactive-water-fukushima-plant-still-flowing-ocean-study-finds/#.XHLIjPnKigA)  
1004 [fukushima-plant-still-flowing-ocean-study-finds/#.XHLIjPnKigA](https://www.japantimes.co.jp/news/2018/03/29/national/seven-years-radioactive-water-fukushima-plant-still-flowing-ocean-study-finds/#.XHLIjPnKigA).
- 1005 47. Livingston H. D., and P. P. Povinec (2000). Anthropogenic marine radioactivity. *Ocean and*  
1006 *Coastal Management*, **43**, 689-712.
- 1007 48. MARIS (2019) Marine Information System, International Atomic Energy Agency, Monaco,  
1008 <https://www.iaea.org/resources/databases/maris>)
- 1009 49. Mecking, S. and M. J. Warner (2001). On the subsurface CFC maxima in the subtropical  
1010 North Pacific thermocline and their relation to mode waters and oxygen maxima, *J. Geophys.*  
1011 *Res.*, **106**, 2156-2202, doi: 10.1029/2001JC000846.
- 1012 50. Men, W, J. He, F. Wang, Fenfen, Y. Wen, Y. Li, J. Huang, and X. Yu, (2015). Radioactive  
1013 status of seawater in the northwest Pacific more than one year after the Fukushima nuclear  
1014 accident, *Scientific Reports*, **5**, doi: 10.1038/srep07757.
- 1015 51. MEXT (2011b). Japanese Ministry of Education, Sports, Science and Technology: Available  
1016 at [http://radioactivity.mext.go.jp/en/1750/2011/08/1750\\_083014.pdf](http://radioactivity.mext.go.jp/en/1750/2011/08/1750_083014.pdf).
- 1017 52. Nie, X., S. Gao, F. Wang, and T. Qu (2016). Subduction of North Pacific Tropical Water  
1018 and its equatorward pathways as shown by a simulated passive tracer, *J. Geophys. Res.*  
1019 *Oceans*, doi: 10.1002/2016JC012305.
- 1020 53. NSCJ (2011). Nuclear Safety Commission of Japan: Trial estimation of emission of  
1021 radioactive materials (I-131, Cs-137) into the atmosphere from Fukushima Dai-ichi nuclear  
1022 power station, Tokyo. Available at: [http://www.nsc.go.jp/NSCenglish/geje/2011\\_0412](http://www.nsc.go.jp/NSCenglish/geje/2011_0412_press.pdf)  
1023 [press.pdf](http://www.nsc.go.jp/NSCenglish/geje/2011_0412_press.pdf).
- 1024 54. Oka, E., and B. Qiu (2012). Progress of North Pacific mode water research in the past decade.  
1025 *J. Oceanogr.*, **69**, 5–20.
- 1026 55. Oka E., and T. Suga (2005). Differential formation and circulation of North Pacific central  
1027 mode water. *J. Phys. Oceanogr.* **35**, 1997–2011.

- 1028 56. Oka, E., L. D. Talley, and T. Suga (2007). Temporal variability of winter mixed layer in the  
1029 mid- to high-latitude North Pacific. *J. Oceanogr.*, **63**, 293–307.
- 1030 57. Oka, E., S. Kouketsu, K. Toyama, K. Uehara, T. Kobatashi, S. Hosoda and T. Suga (2011).  
1031 Formation and subduction of Central Mode Water based on profiling float data, 2003–08. *J.*  
1032 *Phys. Oceanogr.* **41**, 113-129, doi: 10.1175/2010JPO4419.1.
- 1033 58. Oka, E., B. Qiu, Y. Takatani, K. Enyo, D. Sasano, N. Kosugi, M. Ishii, T. Nakano, T. Suga  
1034 (2015). Decadal variability of Subtropical Mode Water subduction and its impact on  
1035 biogeochemistry. *J. Oceanogr.* **71**, 389–400, doi: 10.1007/s10872-015-0300-x.
- 1036 59. ORO (2013). Our Radioactive Ocean, Center for Marine and Environmental Radiation,  
1037 Woods Hole, MA. <http://www.ourradioactiveocean.org/>.
- 1038 60. Pike, S. M., K. O. Buesseler, C. F. Breier, H. Dulaiova, K. Stastna, and F. Šebesta (2012).  
1039 Extraction of cesium in seawater off Japan using AMP-PAN resin and quantification via  
1040 gamma spectroscopy and inductively coupled mass spectrometry. *J. Radioanal. Nucl. Chem.*,  
1041 doi:10.1007/s10967-012-2014-5.
- 1042 61. Povinec, P. P., K. Hirose and M. Aoyama (2012). Radiostrontium in the western North  
1043 Pacific: characteristics, behavior, and the Fukushima impact. *Environ. Sci. Technol.*, **46**, doi  
1044 10.1021/es301997c.
- 1045 62. Qiu, B., P. Hacker, S. Chen. K. A. Donohue, D. R. Watts, H. Mitsudera, N. Hogg and S. R.  
1046 Jayne (2006). Observations of the Subtropical Mode Water Evolution from the Kuroshio  
1047 Extension System Study. *J. Phys. Oceanogr.*, **36**, 457-473.
- 1048 63. Qu, T., H. Mitsudera, and B. Qiu (2001). A Climatological View of the Kuroshio/Oyashio  
1049 System East of Japan, *J. Phys. Oceanogr.*, **31**, 2575-2589.
- 1050 64. Rainville, L., S. R. Jayne, and M. F. Cronin (2014). Variations of the North Pacific  
1051 subtropical mode water from direct observations, *J. Climate*, **27**, 2842–2860, doi:  
1052 10.1175/JCLI-D-13-00227.1
- 1053 65. [RIAM \(2017\). Research Institute of Applied Mechanics, Kyushu University ASUKA](http://www.riam.kyushu-u.ac.jp/oed/asuka/alt/ASUKA_transport_19921007_20100313_20110129.dat)  
1054 [transport time series http://www.riam.kyushu-](http://www.riam.kyushu-u.ac.jp/oed/asuka/alt/ASUKA_transport_19921007_20100313_20110129.dat)  
1055 [u.ac.jp/oed/asuka/alt/ASUKA\\_transport\\_19921007\\_20100313\\_20110129.dat](http://www.riam.kyushu-u.ac.jp/oed/asuka/alt/ASUKA_transport_19921007_20100313_20110129.dat)
- 1056 66. Rossi, V., E. V. Seville, A. S. Gupta, V. Garçon, M. H. England (2013). Multi-decadal  
1057 projections of surface and interior pathways of the Fukushima Cesium-137 radioactive  
1058 plume. *Deep-Sea Res. I.*, **80**, 37–46.
- 1059 67. Rossi, V., E. Van Seville, A. Sen Gupta, V. Garçon and M. H. England (2014). Corrigendum  
1060 to "Multi-decadal projections of the surface and interior pathways of the Fukushima Cesium-  
1061 137 radioactive plume", *Deep Sea-Res. I.*, **93**, 162–164, doi:10.1016/j.dsr.2014.08.007
- 1062 68. Rypina, I. I., S. R. Jayne, S. Yoshida, A. M. Macdonald, E. Douglass, and K. O. Buesseler  
1063 (2013). Short-term dispersal of Fukushima-derived radionuclides off Japan: Modeling efforts  
1064 and model-data intercomparison. *Biogeosciences*, **10**, 1517–1550 , doi:10.5194/bgd-10-1517-  
1065 2013.

- 1066 69. Rypina, I. I., S. R. Jayne, S. Yoshida, A. M. Macdonald, E. Douglass, and K. O. Buesseler  
1067 (2014). Drifter-based estimate of the 5-year dispersal of Fukushima-derived radionuclides, *J.*  
1068 *Geophys. Res.*, **119**, 8177–8193, doi:10.1002/2014JC010306.
- 1069 70. Saito, H., T. Suga, K. Hanawa, and T. Watanabe (2007). New type of pycnostad in the  
1070 western subtropical-subarctic transition region of the North Pacific: Transition region mode  
1071 water. *J. Oceanogr.*, **63**, 589–600.
- 1072 71. Saito, H., T. Suga, K. Hanawa, and N. Shikama (2011). The Transition Region Mode Water  
1073 of the North Pacific and its rapid modification. *J. Phys. Oceanogr.*, doi:  
1074 10.1175/2011JPO4346.1.
- 1075 72. Šebasta, F. (1997). Composite sorbents of inorganic ion-exchangers and polyacrylonitrile  
1076 binding matrix-I. Methods of modification of properties of inorganic ion-exchangers for  
1077 application in column packed beds. *J. Radioanal. Nucl. Chem.*, **1**, 77-88.
- 1078 73. Smith, J. N., R. M. Brown, W. J. Williams, M. Robert, R. N. Nelson, and S. B. Moran (2015).  
1079 Arrival of the Fukushima radioactivity plume in North American continental waters. *Proc.*  
1080 *Nat. Acad. Sci.*, **112** 5.1310-1315, doi:10.1073/pnas.1412814112.
- 1081 74. Smith, J., V. Rossi, K. Buesseler, J. Cullen, J. Cornett, R. Nelson, A. Macdonald, R. Marie  
1082 and J. Kellogg (2017). Time series measurements of the transport of the Fukushima  
1083 radioactivity plume through the northeast Pacific Ocean, *Environmental Science &*  
1084 *Technology*, doi: 10.1021/acs.est.7b02712.
- 1085 75. Smith, W.H.F., and D. T. Sandwell (1997). Global seafloor topography from satellite  
1086 altimetry and ship depth soundings. *Science*, **277**, 1957-1962.
- 1087 76. Steinhäuser, G. A. Brandl, and T. E. Johnson (2014). Comparison of the Chernobyl and  
1088 Fukushima nuclear accidents: A review of the environmental impacts, *Science of the Total*  
1089 *Environment*, **470–471**, 800–817.
- 1090 77. Stohl, A., P. Seibert, G. Wotawa, D. Arnold, J. F. Burkhart, S. Eckhardt, C. Tapia, A. Vargas,  
1091 and T. J. Yasunari (2012). Xenon-133 and caesium-137 releases into the atmosphere from the  
1092 Fukushima Dai-ichi nuclear power plant: Determination of the source term, atmospheric  
1093 dispersion, and deposition, *Atmos. Chem. Phys.*, **12**, 2313–2343.
- 1094 78. Suga, T., and K. Hanawa (1995). The subtropical mode water circulation in the North  
1095 Pacific. *J. Phys. Oceanogr.*, **25**, 958–970.
- 1096 79. Suga, T., K. Motoki, Y. Aoki, Y., and A. M. Macdonald (2004). The North Pacific  
1097 Climatology of Winter Mixed Layer and Mode Waters, *J. Phys. Oceanogr.*, **34**, 1. 3–22,  
1098 2004.
- 1099 80. Taguchi, B and N. Schneider (2014). Origin of Decadal-Scale, Eastward-Propagating Heat  
1100 Content Anomalies in the North Pacific. *J. Climate*, **27**, 7568-7586. doi:10.1175/JCLI-D-13-  
1101 00102.1
- 1102 81. Talley, L. D. (1988). Potential vorticity distribution in the North Pacific, *J. Phys. Oceanogr.*,  
1103 **27**, 89–106.
- 1104 82. [Tazoe H., H. Obata, M. Tomita, S. Nomura, J. Nishioka, T. Yamagata, Z. Karube, and M.](#)  
1105 [Yamada \(2017\).](#) Novel method for low level Sr-90 activity detection in seawater by

- 1106 combining oxalate precipitation and chelating resin extraction. *Geochemical Journal*, **51**,  
1107 193-197, doi: 10.2343/geochemj.2.0441
- 1108 83. TEPCO (2011). Tokyo Electric Power Company: <http://www.tepco.co.jp/en/press/corp->  
1109 [com/release](http://www.tepco.co.jp/en/press/corp-com/release).
- 1110 84. TEPCO (2017). Tokyo Electric Power Company: <http://www.tepco.co.jp/en/nu/fukushima->  
1111 [np/fl/smp/index-e.html](http://www.tepco.co.jp/en/nu/fukushima-np/fl/smp/index-e.html).
- 1112 85. Tsubono, T., K. Misumi, D. Tsumune, F. O. Bryan, K. Hirose, and M. Aoyama (2016).  
1113 Evaluation of radioactive cesium impact from atmospheric deposition and direct release  
1114 fluxes into the North Pacific from the Fukushima Daiichi nuclear power plant. *Deep-Sea Res.*  
1115 *I.* **115**, 10-21.
- 1116 86. Tsumune, T., M. Aoyama, T. Tsubono, K. Misumi and Y. Tateda (2017). Estimations of  
1117 direct release rate of  $^{137}\text{Cs}$  and  $^{90}\text{Sr}$  to the ocean from the Fukushima Dai-ichi Nuclear  
1118 Power Plant for five-and-a-half years. *Geophys. Res. Abstracts*, **19**, EGU2017-12202, 2017  
1119 EGU General Assembly, Vienna Austria.
- 1120 87. United Nations (2000). Exposures to the public from man-made sources of radiation, in  
1121 Sources and Effects of Ionizing Radiation. United Nations Scientific Committee on the  
1122 Effects of Atomic Radiation, UNSCEAR 2000 Report to the General Assembly, with  
1123 scientific Annexes, **1**, pp. 158–291, U. N., New York.
- 1124 88. Whalen, C. B., L. D. Talley, and J. A. MacKinnon (2012). Spatial and temporal variability of  
1125 global ocean mixing inferred from Argo profiles. *Geophys Res. Lett.*, **39**, L18612,  
1126 doi:10.1029/2012GL053196.
- 1127 89. Yoshida, S., A. M. Macdonald, S. R. Jayne, I. I. Rypina and K. O. Buesseler (2015).  
1128 Observed eastward progression of the Fukushima  $^{134}\text{Cs}$  signal across the North Pacific,  
1129 *Geophys. Res. Lett.*, doi: 10.1002/2015GL065259.
- 1130 90. You, Y., N. Sugimoto, M. Fukasawa, I. Yasuda, I. Kanekos, H. Yoritaka, and M. Kawamiy  
1131 (2000). Roles of the Okhotsk Sea and Gulf of Alaska in forming the North Pacific  
1132 Intermediate Water. *J. Geophys. Res.*, **95**, 3253-3280.